Low voltage miniaturized ion thrusters

Sourav Mukherjee

Department of Electrical & Computer Engineering

McGill University

Montreal, Quebec, Canada

December, 2023

A thesis submitted to McGill University in partial fulfillment of the requirements of the degree of

Master of Science

(First published on 15th December, 2024)

Abstract

An ion thruster or EHD (Electrohydrodynamic) blower is an electromechanical transducer that converts electrical energy into airflow or thrust. Traditional ion thrusters require tens of thousands of voltages to operate, which hinders the commercial application of the technology. This research targets the miniaturization of ion thrusters, with the aim of significantly reducing the operational voltage. Recently, miniaturized ion thrusters have been considered to build small flying robots, often called "ionocrafts", with no moving parts and almost silent operation. The small form factor and low power targeted here also make a unique case for solid-state cooling.

In this thesis, a novel ion thruster design with probe needle architecture has been thoroughly examined. The design capitalizes on a PCB-level framework that gives the ability to customize most geometrical parameters that severely impact the performance of the system. A corona inception voltage (CIV) below 1500 V has been achieved with the architecture for the smallest inter-electrode gap. A maximum air velocity of $\sim$ 6 m/s was achieved in this architecture. With just 8.3 mm $\times$ 8.3 mm overall size, the device produces

one of the highest airflow and thrust densities ($> 40\ N/m^2$) ever reported at such low voltage and scale.

Another novel design uses microfabrication to fabricate silicon microwires with a small tip radius of 2.5 μm. The design uses 1 mm $\times$ 1 mm cut silicon dies integrated with the PCB-level framework previously mentioned. The microwire jungle reduces the CIV to under 1000 V. Sustained corona generation at such low voltage ushers extraordinary possibilities.

The key to further operational voltage reduction lies in further miniaturization, especially through the reduction of the emitter radius. The research also demonstrates a method for the controlled fabrication of vertically aligned silicon nanowires (SiNWs) using EBL (electron beam lithography) and DRIE (deep reactive ion etching). Characterization of the fabricated nanowires shows tight control with the fabricated diameter error being under 4% and a pitch error under 1.8% of the EBL mask for 300 nm radius nanowires.

Finally, a novel chip-level fully integrated fabrication technique has been proposed which potentially opens up the possibility for sub-millimeter scale corona wind driven micro air vehicles (MAVs). The device parameters remain widely tunable with the capability of customizing the inlet/outlet holes, the number of emitters and their arrangement, the emitter radius, the inter-electrode gap, etc.

Abrégé

Un propulseur ionique ou ventilateur EHD (électrohydrodynamique) est un transducteur électromécanique qui convertit l'énergie électrique en débit d'air ou en poussée. Les propulseurs ioniques traditionnels nécessitent des dizaines de milliers de tensions à fonctionner, ce qui entrave le déploiement commerciale de la technologie. La recherche porte sur la miniaturisation des propulseurs ioniques, ce qui réduit considérablement la tension de fonctionnement. Récemment, des propulseurs ioniques miniaturisés ont été envisagés pour construire de petits robots volants, souvent appelés "ionocrafts", sans pièce mobile et fonctionnant presque silencieusement. De plus, le petit facteur de forme et la faible consommation constituent un argument unique en faveur du refroidissement par semi-conducteurs.

Dans cette thèse, une nouvelle conception de propulseur ionique avec une architecture d'aiguille de sonde a été examinée en profondeur. La conception capitalise sur un cadre au niveau du PCB qui permet de personnaliser la plupart des paramètres géométriques ayant un impact important sur les performances du système. Une tension d'induction corona (CIV)

inférieure à 1500 V a été obtenue avec l'architecture pour le plus petit écart inter-électrodes. Une vitesse maximale de l'air de $\sim$ 6 m/s a été atteinte avec cette architecture. Avec une taille globale de seulement $8,3$ mm $\times$ $8,3$ mm, l'appareil produit un débit d'air et une densité de pousée ($> 40\ N/m^2$) parmis les plus élevées jamais reportées à des niveaux aussi bas en tension et en échelle.

Une autre nouvelle conception utilise la microfabrication pour fabriquer des microfils de silicium avec un petit rayon de pointe de $2,5\ \mu m$. La conception utilise des matrices en silicium découpées en morceaux de 1 mm $\times$ 1 mm et intégrées au cadre de niveau PCB mentionné précédemment. La jungle des microfils réduit le CIV à moins de 1000 V. La génération soutenue de couronnes à une tension aussi basse ouvre la voie aux possibilités extraordinaires.

La clé d'une réduction supplémentaire de la tension de fonctionnement réside dans une miniaturisation accrue, notamment via la réduction du rayon de l'émetteur. La recherche démontre également une méthode de fabrication contrôlée de nanofils de silicium alignés verticalement (SiNW) à l'aide de l'EBL (lithographie par faisceau d'électrons) et du DRIE (gravure ionique réactive profonde). La caractérisation des nanofils fabriqués montre un contrôle strict avec une erreur de diamètre fabriqué inférieure à 4% et une erreur de pas qui est inférieure à $1,8\%$ du masque EBL pour des nanofils de rayon de 300 nm.

Enfin, une nouvelle technique de fabrication entièrement intégrée au niveau de la puce a été proposée, ce qui ouvre potentiellement la possibilité de créer des micro-véhicules aériens

(MAV) entraînés par le vent corona à l'échelle submillimétrique. Les paramètres de l'appareil restent extrêmement réglables avec la possibilité de personnaliser les trous d'entrée/sortie, le nombre d'émetteurs et leur disposition, le rayon de l'émetteur, l'espace inter-électrodes, etc.

Acknowledgements

I would like to express my heartiest gratitude to my supervisor Prof. Mourad N. El-Gamal for his continuous guidance throughout my time in McGill. I am extremely grateful to Dr. Mohannad Y. Elsayed and Dr. Hani H. Tawfik from MEMS Vision International Inc. for their support in my journey.

I am also thankful to the cleanroom technicians at the McGill Nanotools Micro and Nanofabrication Facility (Nanotools), and at the GCM Lab of Polytechnique Montréal for their training and suggestions on the microfabrication processes.

Thank you, Mom and my dear sister for your tolerance. I have always sidelined your expectations, trying to be in my cocoon.

Last but not least, I'd like to acknowledge Maninder Bir Singh Gulshan and Shahroza Nahrin for always being there for me!

Contribution to Original Knowledge

Corona discharge at the sub-millimeter inter-electrode gap is of special interest to researchers because of its potential impact on performance improvement. This work investigates corona wind generation for different sub-millimeter inter-electrode gaps. The air velocity and thrust density achieved are among the highest, if not the highest ever reported in the literature. Moreover, a PCB-level framework is demonstrated to achieve sub-millimeter gaps without cleanroom facilities.

Traditional ion thrusters require extremely high voltages to operate. One of the important achievements of this work is to successfully reduce the Corona Inception Voltage (CIV) under 1.5 kV using a probe needle architecture.

The work also demonstrates microfabricated emitters to further reduce the operational voltage under 1000 V. Methods to controllably fabricate silicon microwires and silicon nanowires are reported here. These methods can be extremely helpful in designing ion thrusters with small emitter tip radii.

Moreover, a novel process flow for chip-level fully integrated ion thruster design has been

proposed. The method eliminates all manual assembly steps and facilitates the control of all major geometric parameters. The device could be used in various semiconductor cooling applications, due to its compatibility with modern microfabrication techniques. It also opens up possibilities for ionic wind powered micro air vehicles (MAVs) with extremely small form factors.

Contribution of Authors

The conceptualization, design, fabrication, testing, data analysis, and drafting have been done by the author of this thesis (Mr. Sourav Mukherjee).

The thesis contains works that are to be submitted for publication in 2 peer-reviewed scientific journals. Dr. Mohannad Y. Elsayed and Dr. Hani H. Tawfik have provided technical suggestions and have reviewed the results and all publication manuscripts.

Prof. Mourad El-Gamal provided overall supervision and guidance throughout the project.

Contents

List of Figures

List of Tables

List of Acronyms

ACT	Asymmetrical Capacitor Thruster.
Al	Aluminum.
CIV	Corona Inception Voltage.
CMOS	Complementary Metal Oxide Semiconductor.
CNT	Carbon Nanotube.
COP	Coefficient of Performance.
Cr	Chromium.
CVD	Chemical Vapor Deposition.
DC	Direct Current.
DRIE	Deep Reactive Ion Etching.
EBE	Electron Beam Evaporation.
EBL	Electron Beam Lithography.
EHD	Electrohydrodynamics.
ESP	Electrostatic Precipitator.

EV	Electric Vehicle.
FEA	Finite Element Analysis.
HF	Hydrogen Fluoride.
HMDS	Hexamethyldisilazane.
HVPS	High Voltage Power Supply.
IC	Integrated circuit.
IoT	Internet of Things.
IPA	Isopropyl Alcohol.
LFM	Linear Feet Per Minute.
MACE	Metal Assisted Chemical Etching.
MAV	Micro Air Vehicle.
MEMS	Microelectromechanical System.
MIBK	Methyl Isobutyl Ketone.
MSD	Multi-stage Ducted.
MTTF	Mean Time To Failure.
NASA	National Aeronautics and Space Administration.
PCB	Printed Circuit Board.
PDN	Power Distribution Network.
PMMA	Polymethyl Methacrylate.
PR	Photoresist.

RIE	Reactive Ion Etching.
SCD	Space Charge Density.
SEM	Scanning Electron Microscope.
SERT	Space Electric Rocket Test.
SiNW	Silicon Nanowire.
SOI	Silicon On Insulator.
TiN	Titanium Nitride.
US	United States.
VLS	Vapor-Liquid-Solid.

Chapter 1

Introduction

Since the dawn of time, mankind has forged the physical phenomena in their benefits, to fuel human civilization. Almost all such technological marvels go through a few landmark innovations that pave the way towards the commercial fruition of the technology. Ionic wind or EHD-based systems, with their tremendous potential in diversified applications, have been known to us for quite some time now, but their commercial application remains extremely limited.

Components of this chapter will be submitted for publication in a peer-reviewed scientific journal [1].

1.1 What is an ion thruster or EHD blower?

In ion thrusters, EHD or Electrohydrodynamic thrust is observed. In such a process, charged particles in collision with neutral particles result in a gas flow often referred to as "ionic wind" or "corona wind". The ionic wind can potentially be used in various applications. The mechanism of a typical EHD system is illustrated in Figure 1.1. Although there can be several variations, a traditional ion thruster is primarily made of two electrodes, one being an emitter and another one a collector, separated by a small gap. In a DC positive corona discharge system, the emitter is connected to the positive polarity, whereas the collector is grounded. When applied with high voltage, the asymmetric electrodes create an electric field gradient, the strength of which depends on the emitter tip radius. The ionized (positively charged particles for positive corona) particles near the emitter tip experience a push towards the collector due to the strong electric field. The charged particles, while moving toward the collector, collide with the neutral particles transferring the momentum and resulting in a wind flow toward the collector. A DC negative corona discharge system is also possible with the negative polarity connected to the emitter. Positive corona generation produces significantly less ozone compared to negative corona, making it our method of interest [2].

In a positive corona discharge mechanism, the inter-electrode gap has two regions namely the ionization region and the drift region. The ionization region is formed close to the emitter tip, causing Townsend avalanche breakdown resulting in sustained plasma generation. In the drift region, positively charged particles (for positive discharge) move toward the collector

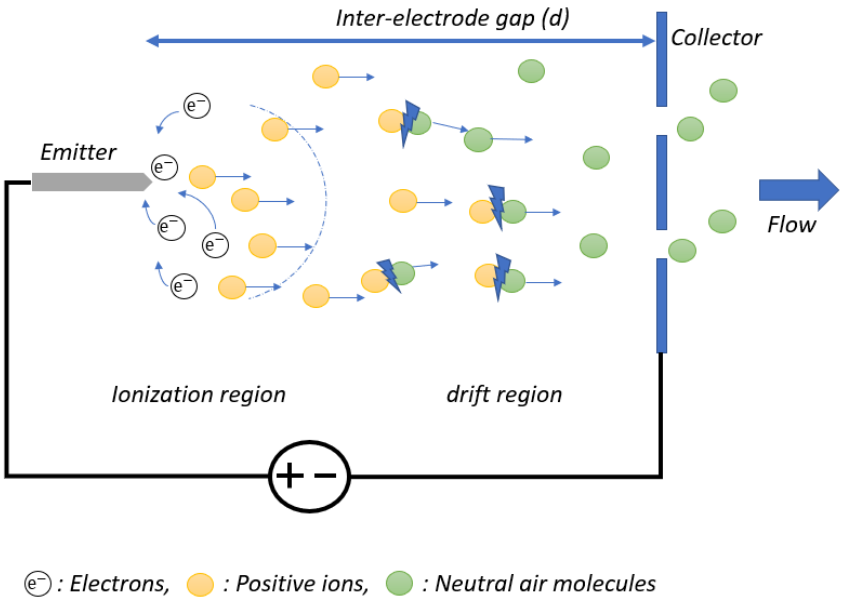

Figure 1.1: A typical EHD system: A needle-to-grid architecture is shown with the ionization and drift regions.

due to the strong electric field. The inter-electrode gap can be filled with air or other gases. Furthermore, the operation of such a device also greatly depends on environmental factors such as pressure, temperature, and humidity [3–6].

1.1.1 The geometry

Ion thrusters are generally made of asymmetric electrodes separated by a certain distance. The coronating electrode, which starts the ionization and generates the plasma, is called the emitter, whereas the other electrode is called the collector. Two key geometric parameters are the emitter tip radius and the inter-electrode gap. Figure 1.2 shows some common EHD

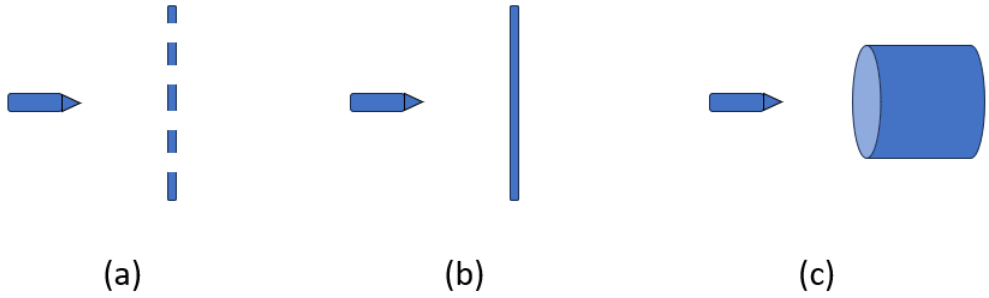

Figure 1.2: Common EHD architectures: (a) Needle-to-grid architecture, (b) Needle-to-plane architecture, (c) Needle-to-ring architecture.

architectures. Needless to say, the architecture can vary significantly depending on several factors. For example, instead of a single emitter, multiple emitters can be used. Also, multiple stages can be stacked together to implement a multi-stage device. Both emitter and collector design and their optimization play key roles in the performance of EHD systems.

1.1.2 Region of operation

The ionization takes place near the sharp electrode, i.e., near the emitter tip when the electric field is greater than a certain threshold value, E_{crit}. After the plasma starts to occur, an increment of supply voltage results in higher current and resultant airflow. After a certain voltage, sparking occurs, exhibiting significantly higher current and no flow. In the sparkover region, the entire gap becomes ionized and conductive, whereas during sustained corona generation only the emitter tip is ionized. Moreover, sparking is detrimental to the

device's durability. Thus, the device must operate in the region between the onset voltage and the sparkover region. The range of voltage between the onset of the corona to the sparkover region heavily depends on the inter-electrode gap and tends to be smaller for small inter-electrode gaps.

1.2 Motivation

Miniaturized ion thrusters have several advantages and can be used in several applications ranging from robotics to solid-state cooling.

1.2.1 Ion thruster: from space to Earth

Ion thrusters or ion engines have long been used primarily in the space industry, with their comparatively large size and huge voltage requirements [7]. Another area of research is to use micro thrusters to position CubeSat satellites accurately in their orbit [8]. Miniaturization and optimization are needed to accommodate small satellites, but the technology doesn't find any practical applications on Earth, primarily because of the extremely high operational voltage requirements. A traditional ion thruster requires tens of thousands of volts to operate, the reduction of which remains a prime challenge. One of the primary focuses of this research is to explore solutions to reduce operational voltages in order to facilitate greater adoption of the technology.

1.2.2 Moore's scaling and the power crisis

In 1965, Gordon Moore - the founder of semiconductor giant Intel, predicted that the number of transistors in a chip would increase exponentially over time. The industry grew catching up with the self-fulfilling prophecy sustainably. The number of transistors increased with the power consumption remaining static. The rosy days for the astonishing semiconductor device scaling came to an end with the demise of Dennard's scaling. After around 2006, the number of transistors on a chip grew with compromising power costs. The increasing power density in modern chips thus requires better heat dissipation techniques. The issue is going to get worse with the advent of AI and the ever-growing demand for more speed. We are at a juncture where humanity desperately needs innovation to deal with the slowing Moore's law and the power crisis.

Rotary fans used for electronic cooling are inefficient in several aspects. Mechanical fans exhibit the following relation [9],

$$Q \propto \omega^1 \phi_F^2 h^1, \tag{1.1}$$

where Q is the flow rate (in m^3/s), ω is the rotation speed (in rad/s), ϕ_F is the fan diameter (in m), and h is the rotor blade height (in m).It clearly shows that the scalability of mechanical fans isn't viable for modern electronics. The flow rate is directly proportional to the blade height, whereas thinner electronic gadgets are what the market needs nowadays. The fan diameter also can't be increased due to space constraints. Higher rotational speed, on the other hand, brings more noise and reliability challenges.

EHD-based blowers are highly customizable in terms of their geometrical features and offer almost silent operation. The authors in [10] explained the scalability of EHD-based blowers and their potential implementation in smaller form factors.

There have been continuous efforts to build innovative cooling solutions for both the IC and PCB levels of heat dissipation, but we are still far from a comprehensive solution that can withstand future needs [11, 12]. Recently, chip-level solid-state fans or miniaturized ion thrusters have garnered much attention due to their great potential as prime cooling devices. One key objective of our research is to generate high airflow at a comparatively lower voltage for possible cooling applications.

1.2.3 Microengines and the future of robotics

Recently, much research has been focused on miniaturizing these devices to build corona discharge-based small flying microbots, often referred to as "ionocrafts" [13, 14]. With no moving parts, these ion thrusters can be highly robust with excellent performance. Ionocrafts can access areas where humans or bigger robots may struggle to reach. This opens up extraordinary capabilities in surveillance, exploration, evacuation, etc. These devices can revolutionize the next generation of communication systems by acting as small mobile IoT (Internet of Things) hubs. Due to their small sizes, mass manufacturing of the devices may become more economical as well.

Nature has inspired researchers for ages. Insect-scale traditional robots have been the

focus of many researchers for decades [15–22]. These devices require many components and suffer from low efficiency and mechanical limitations. Ionocraft, on the other hand, offers a better proposition with its robust (no moving part), almost-silent operation. In this work, we will also examine ways to improve key propulsion parameters such as thrust density, thrust-to-power ratio, etc.

Although there are other applications of the DC corona discharge technology, such as Electrostatic precipitator (ESP) or air purifiers, which are widely popular [23–26], the focus here remains on solid-state cooling and solid-state propulsion.

1.3 Thesis organization

The thesis consists of 7 chapters. Chapter 1 introduces the reader to ion thrusters and points out the fundamental challenges related to the technology that drives the motivation for the research.

Chapter 2 provides an extensive literary survey. The literature gives the historical context and covers the recent advancements in detail. The focus remains primarily on propulsion and cooling applications. Small form factor miniaturized ion thrusters occupy a major part of the literature.

Chapter 3 covers the mathematical background of the technology and provides the parametric analysis of key geometrical features (i.e., the gap and the emitter radius) using a COMSOL model. The chapter argues for miniaturization in order to enable

high-performance, application-specific deployment of the technology.

Chapter 4 is the core of this research and proposes 2 novel ion thruster designs. The probe needle (PN) based architecture provides airflow as high as $\sim$ 6 m/s with CIV under 1500 V. Another design with microfabricated die-level microwires further reduces the CIV.

In Chapter 5, a fabrication method for vertically aligned silicon nanowires has been demonstrated, which can potentially further reduce the operational voltage. The characterization and analysis show extreme control of the diameter and pitch.

Chapter 6 covers possible future work and highlights the major roadblocks. A novel chip-level ion thruster design has been showcased. The proposed method can generate sub-millimeter scale ion thrusters. With its extreme tunability in terms of geometrical parameters, the proposed technique opens up a plethora of opportunities.

Finally, in chapter 7, the concluding remarks are shared.

Chapter 2

Literature Review

2.1 Early works

One of the first observations of electrostatic forces and sparking was documented by Otto von Guericke in 1672, although the phenomenon remained unexplained at that time [27]. Francis Hauksbee, in 1709, first indicated ionic wind when a charged tube near his face caused a blowing sensation [28, 29]. The work invoked a special interest in the subject matter among scientists, including Sir Issac Newton [29]. In his work in 1838, Faraday explained the ionic wind phenomenon as a result of the collision between charged and neutral air particles, hinting towards the momentum-transfer process [29]. It was probably the earliest accurate explanation of the ionic wind phenomenon. More than a century later, Robinson, in 1961, was the first to properly quantify the ionic wind generated due to corona discharge [30].

Robinson achieved an airflow of 4 m/s at around 50 kV power supply and reported a low electrokinetic energy conversion efficiency. Since the mid-twentieth century, several works have been focused primarily on propulsion and cooling applications.

2.1.1 Ionic wind in electric propulsion

Thomas Townsend Brown is a controversial name from the last century that cannot be ignored while talking about corona-driven electric propulsion. While working on high voltage asymmetric capacitors, Brown noted a net force generated in one electrode's direction, the capacitors which are now known as ACT (Asymmetrical Capacitor Thrusters) [31, 32]. Brown named this phenomenon "Biefeld-Brown effect", and his patent in 1960 explained how his "thrust producing apparatus" could be used for various propulsion applications [33]. Brown claimed that the device managed to impact the gravitational field of Earth, causing an anti-gravity effect or 'electrogravitics', but his claim was never proven and garnered heavy criticism. Although his understanding of ionic wind might be questionable, his experimental works sparked renewed interest in electric propulsion. Around the same time, NASA (National Aeronautics and Space Administration) started to show interest in this technology with Kaufman's ion thruster showing the first electric propulsion in space in the 'Space Electric Rocket Test' (SERT I) mission. Subsequent experiments during SERT II showed extreme success with the newly developed thruster technology, which worked for thousands of hours. The success made the

use of ion thrusters in space extremely common [34].

The device architecture of an ion thruster plays a key role in optimizing the performance of EHD systems. G. E. Hagen, in his 1964 patent, showed several wire-to-grid architecture thrusters, operating at 15000 V [35]. Interestingly, several research works in recent times show staggering similarities to these wire-to-grid architectures. Apart from the general architecture, researchers also started to look into other factors, such as the number of emitters. Researchers from UC Davis in 1967 analyzed the flow and thrust for a multi-emitter negative corona system, but the maximum power efficiency achieved was only around 1% [36].

In space, a propellant is used as a medium, whereas air-medium propulsion remains the focus of interest for researchers during the last few decades. Masuyama et al. worked on single and dual-stage ion thrusters with large inter-electrode gaps (in a few centimeters) investigating thoroughly the thrust and thrust-to-power ratio [37]. They achieved a thrust-to-power ratio of 110 mN/W in their experiments, which is extremely high. They also showed that there is a tradeoff between thrust and thrust-to-power ratio. Several similar works have been presented with centimeter-scale inter-electrode gaps and high onset voltages [38–40].

In recent times, there have been several works on ionic propulsion where the traditional 'lifter' design has been the go-to architecture for researchers [41–45]. Just when the field seemed to become static, researchers at MIT demonstrated in 2018 the first solid-state

propulsion, which attracted extraordinary media coverage [46]. The work galvanized the field, igniting renewed interest from researchers to hobbyists.

2.1.2 Ionic wind in solid-state cooling

One of the earliest works on corona wind-driven electronic cooling came from Yang et al., with a maximum flow of 4 m/s or 800 LFM (linear feet per minute) [47]. The corona inception voltage remained extremely high at 5.2 kV. In 2008, Yang's co-author Jewell-Larsen published a paper which showed 1.1 m/s average air velocity at 8 kV operational voltage for a wire-to-grid design with a gap of 9 mm and emitter radius of 50 μm [48]. Just next year, he showcased another prototype to cool laptops, showing superior performance compared to stock fans. The design possessed a voltage converter that converted a 12 V power supply to approximately 3000 V for the operation, and the authors specifically mentioned the integration challenge of the converter [49].

The idea of a miniaturized EHD cooling system also attracted the attention of big corporations. Apple Inc. was granted a patent on a PCB-level ionic cooling system in 2012 [50]. The corona-driven electronic cooler proposed is supposed to work at a very high voltage, which inevitably brings more circuitry, power consumption, and complexity which in a larger context hardly brings any fruit.

2.2 Trends to go small

Dan Schlitz et al. in 2008 designed a solid-state fan capable of cooling a 20 W chip with a maximum pressure head of 42 Pa [51]. The cooling device weighed about 4 gm, had a size of 1800 mm^3, and a power rating of 1.6 W. Although the operational voltage remained more than 1700 V, this is one of the first works towards miniaturization. It was clear from initial miniaturization efforts that miniaturization can significantly bring down the operational voltage, and the need to use microfabrication processes was identified. Still, there have been very few works that exploited microfabrication techniques to build miniaturized devices. Hsu was the first to try miniaturization using traditional microfabrication techniques. Using an SOI wafer, a cantilever-to-plane architecture was created using DRIE and RIE, where the cantilever works as the emitter with a backside curvature radius of 0.5 μm [52]. The corona onset voltage was around 2 kV for the smallest gap of 1 mm. The device was placed on a hot surface, and a surface temperature reduction of $25°C$ was measured at an operational voltage of 8.5 kV. In his other design, a similar cantilever with a high aspect ratio coronating silicon pillar was used [53]. A maximum increase of the average convective heat transfer coefficient of 58.6 W/m^2K was achieved at 7.5 kV for an inter-electrode gap of 5 mm. Ong from Case Western Reserve University designed a device using photolithography and copper electroplating based on a wire-to-grid architecture with a tip-to-collector gap of 1 mm and an emitter tip diameter of ~ 20 μm resulting in a COP (coefficient of performance) of 20.6 [54, 55]. At an operational voltage of -1.35 kV, $4°C$ temperature reduction was observed.

The low operational voltage was a significant improvement from previous works. Ong also designed an array of 6 devices and concluded that the cooling performance was better than conventional CPU fans [56].

Daniel Drew worked extensively during his PhD on miniaturized ion thrusters for propulsion applications. His work in [57] is one of the earliest efforts to use a microfabricated device as a thruster. The device consisted of a single emitter and employed a wire-to-grid geometry, having a mass of only 2.5 mg, with 100 mm^3 overall size. A maximum thrust of 0.5 mN was achieved. Although the corona onset voltage and hence the operational voltage remained high. An optimized emitter and smaller gap (500 μm) resulted in a significant reduction in the corona onset voltage [58]. In [59], a lift-off was demonstrated with a 10 mg, 1.8 cm $\times$ 1.8 cm quad-thruster having a thrust-to-weight ratio of approximately 10. While using EHD thrusters, one line of thought is to use voltage converters to provide high voltage. This doesn't only require additional complex circuitry, but it also adds additional weight and consumes real estate. On the contrary, Drew, Ong, etc., have diverted to make low-voltage devices by miniaturization, reducing the need for sophisticated converters. Efforts have also been placed to manufacture similar miniaturized thrusters without using cleanroom facilities. In [14], a laser-fabricate thruster inspired by Drew's work resulted in higher thrust but a similar thrust-to-weight ratio.

2.3 The boundary that needs to be pushed

It is evident from the literature that a high operational voltage remains the primary obstacle. Moreover, a small form factor is also extremely desirable for specialized solid-state cooling applications. As the geometrical features impact the overall performance profusely, the customizability of geometrical features, including but not limited to the emitter number, emitter radius, inter-electrode gap, and inlet/outlet hole size is highly advantageous, which is always lacking in the literature. Well-defined and confined channels reduce loss and improve overall performance, which again is hardly seen in designs in the literature.

The literature also indicates the path towards miniaturization, specifically by reducing the emitter radius and gap, a logical step ahead to deal with it. If we talk about sub-millimeter inter-electrode gap corona discharge, Tirumala's work deserves a mention [60]. Tirumala showed experimentally how a small gap leads to a small corona onset voltage. Also, for different applications, works have repeatedly shown corona discharge at a lower voltage for small gaps. In [61], authors were able to generate plasma at 50 V with an inter-electrode gap of less than 3 μm for microplasma transistor application. Thus, sub-millimeter inter-electrode gap corona devices are highly desirable and expected to produce good results.

Subsequent chapters cover in detail the need for miniaturization and propose a few miniaturized architectures aiming to tackle the aforementioned challenges.

Chapter 3

Theoretical Background and Numerical Modeling

Part of this chapter will be submitted for publication in a peer-reviewed scientific journal [1].

3.1 Introduction

Ion thrusters have historically been investigated primarily in space applications. But recently, there has been some interest in miniaturized ion thrusters, especially because of their small form factors and low operational voltages. This chapter investigates the impact of the emitter radius (r), the inter-electrode gap (d), and most importantly, the gap-to-emitter radius ratio, i.e., the d/r ratio, while designing an air-medium miniaturized ion thruster or EHD blower.

A lower corona inception voltage (CIV) and higher air flow are two of the most desirable parameters in designing EHD blowers, which we analyzed in this chapter. The analysis, backed by literature data, unfolds the fact that the d/r ratio has a far greater impact on the design in comparison to the impact of 'd' and 'r' when considered separately, specifically at the smaller gap and radius values. Furthermore, an FEA (using COMSOL Multiphysics) model has been presented, which supports the argument for miniaturization. The FEA results show a huge improvement in operational voltage reduction and match the analytical model without significantly sacrificing the airflow. There has been a limited amount of work on the miniaturization of ion thrusters. This work aims to provide a comprehensive understanding of the possibilities and limitations of miniaturization.

In our analysis, we have considered an air-medium, single-stage, atmospheric pressure ion thruster, which is a practical approximation of its potential working conditions in day-to-day applications.

F. W. Peek, in the early 20th century, carried out extensive experimental research on corona discharge relating to high-voltage transmission lines. Peek's equation provides the minimum electric field required for corona discharge for parallel wire electrode architecture. The threshold or critical electric field (E_{crit}) at the point of onset of the corona is defined by equation (3.1) for smooth emitter surface at ambient temperature and atmospheric pressure [62].

$$E_{crit} = g_0 \left(1 + \frac{0.301}{\sqrt{r}}\right), \tag{3.1}$$

where g_0 is the electric breakdown strength of air (31 kV/cm) and 'r' is the emitter tip radius. The empirical equation also shows that the electric field strength solely depends on the emitter wire tip radius.

Peek's equation focused mainly on the parallel wire case whereas, for the wire-to-plane case, the electric field (for an applied voltage, V) at the emitter tip can be written as [63,64],

$$E_{crit} = \frac{V}{rln\left(\frac{2d}{r}\right)} \ . \tag{3.2}$$

From equation (3.1) and equation (3.2), we get the onset voltage of the corona, commonly known as the corona inception voltage (CIV) or the corona onset voltage or the critical voltage (V_{crit}). The CIV indicates the starting phase of sustained corona generation [64].

$$CIV \ or \ V_{crit} = m_v g_0 r \left(1 + \frac{0.301}{\sqrt{r}}\right) \ln\left(\frac{2d}{r}\right), \tag{3.3}$$

where m_v indicates the surface roughness of the emitter, which is 1 for a smooth surface. The inter-electrode gap (d) and the emitter radius (r) should be in centimeters. The equation highlights the importance of the emitter radius and the inter-electrode gap in designing a low operating voltage corona system.

The corona discharge current can be approximated using Townsend's current-voltage relationship [65],

$$I_{corona} = CV(V - V_{crit}), \tag{3.4}$$

where 'C' is a coefficient (unit: A/V^2) that depends on the geometry and the ion mobility, and 'V' is the operational voltage. The discharge current thus heavily depends on the structural features of the design.

The previous relationship formulated in equation (3.4) is valid until the gas medium between the two electrodes reaches the breakdown voltage, which is predicted by Paschen's law. This breakdown voltage is a function of the inter-electrode gap and pressure. Although it has been rigorously validated experimentally, it fails to predict atmospheric pressure air-medium discharge with small gaps accurately. Recently, a revised version of the law, the 'Modified Paschen's curve' has been able to accurately show that continuous decrement in the inter-electrode gap can indeed reduce the breakdown voltage of the medium [66, 67]. The modified Paschen's curve has been verified by many experimental works already.

Solid-state propulsion using corona discharge remains one of the primary applications of the technology. The idea is to use the corona-generated airflow or thrust to lift heavier-than-air objects. In this regard, works at MIT [46] and the work by Drew [57] deserve credit for stirring renewed interest in this domain. We have already covered these works in the literature review. Another key application for corona discharge is in what is called an EHD blower, where the outlet airflow is used for cooling and drying purposes. There has been a continuous effort to build EHD cooling systems with high transduction efficiency, and an efficiency of more than 8 CFM/W has already been achieved [68]. Apart from efficiency, the form factor is extremely important for such cooling applications as well. Traditional

fans fail to serve the ever-growing need for thinner and lightweight laptops. Nels, in 2011, explained the scaling laws for EHD-based fans [10]. He argued for EHD-based fans as the traditional fans are noisy and require higher diameter and height for greater airflow, which is not sustainable or desirable.

In section 3.1, we have presented some important theories related to corona discharge and its most common applications. In section 3.2, we have analyzed the impact of key geometrical features (i.e., the emitter radius and inter-electrode gap) in light of some literature data. A COMSOL model is proposed to investigate the impact of miniaturization for a wire-to-grid architecture design in section 3.3. Subsequently, we analyze the FEA results in section 3.4. Section 3.5 is dedicated to the discussion on the potential of the technology and concluding remarks.

3.2 Impact of the key geometrical features

3.2.1 Impact of the inter-electrode gap and emitter radius

While designing a corona discharge system, the two most important design choices are the emitter radius (r) and the electrode gap (d). In this section, we have discussed the impact of gap and emitter radius on the CIV based on the analytical model validated by previous literature data [57, 60, 69–72].

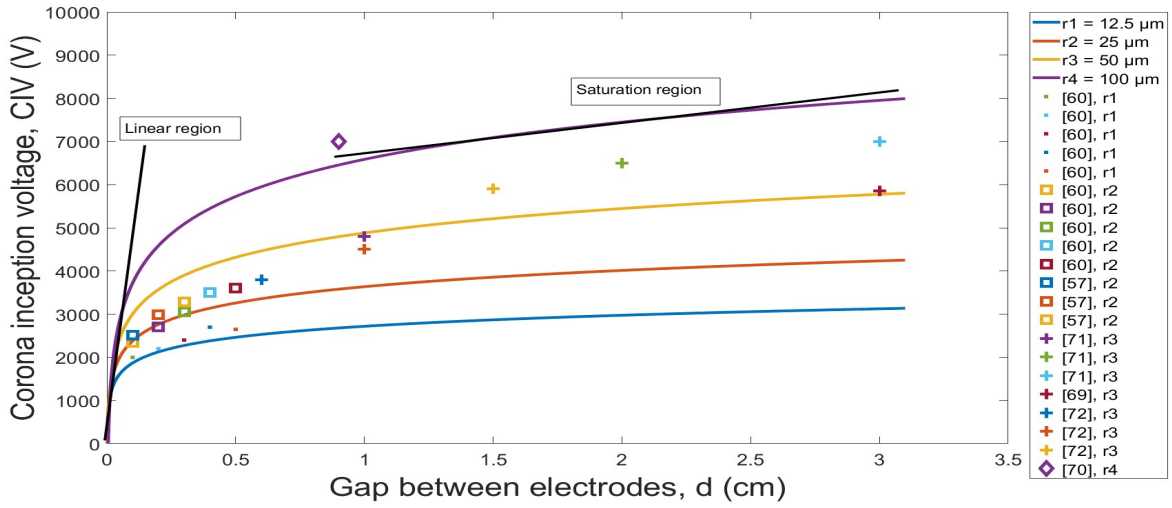

Figure 3.1: Corona inception voltage (CIV) as a function of varying electrode gap (d) based on equation (3.3). Scatter plots from the literature [57, 60, 69–72] validate the theoretical model.

(1) CIV vs d (at fixed r)

The plot for CIV as a function of the inter-electrode gap (for fixed emitter radius) is shown in Figure (3.1) based on equation (3.3). Many previous works have validated this analytic model. The graph shows that, for small gaps, the inception voltage changes rapidly, but for larger gaps, the CIV changes rather slowly. The plot thus can be approximated into two regions:

(a) Linear region: The CIV increases almost linearly with the gap. The linear region lasts longer when the emitter radius is larger, whereas the saturation region sets in early when the emitter radius is smaller. This gives us an important design insight. For designs with a small emitter radius, which seems to be an appropriate choice in order to reduce the CIV, a

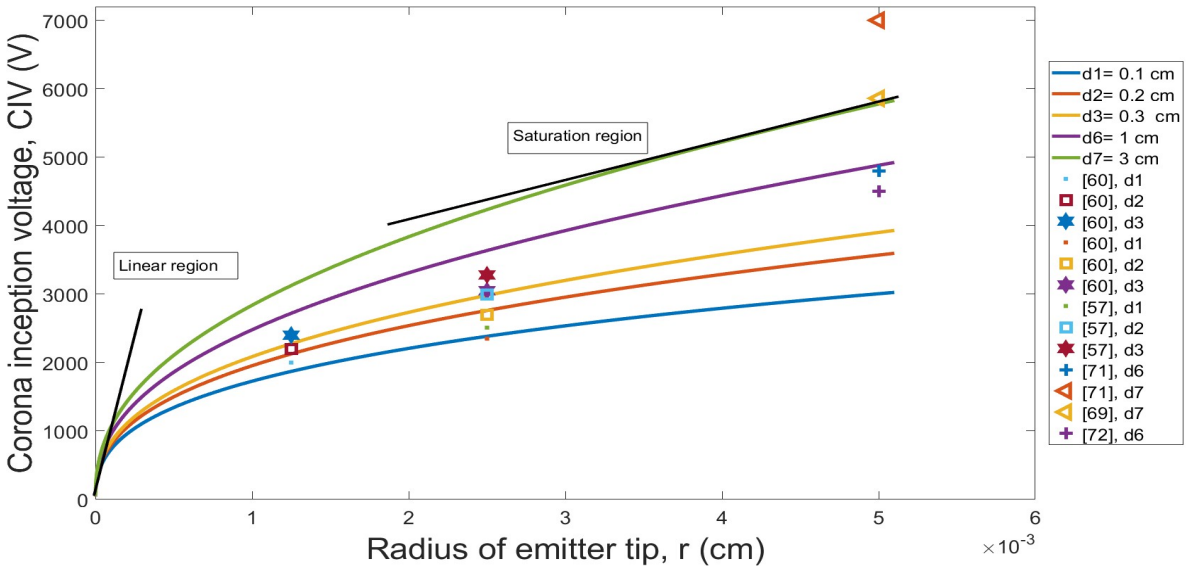

Figure 3.2: Corona inception voltage (CIV) as a function of varying emitter tip radius (r). Scatter plots from the literature [57, 60, 69, 71, 72] validate the theoretical model.

little change in the inter-electrode gap greatly changes the expected CIV when the gap is in the linear region.

(b) Saturation region: With a large inter-electrode gap, the CIV increases with a very small slope. In this region, a little change in the gap doesn't change the CIV significantly.

(2) CIV vs r (at fixed d)

Similar to the relationship between the CIV and the gap, the plot of the CIV as a function of the emitter radius also has 2 regions. The linear region lasts longer for bigger gaps, which also tends to give a higher CIV.

It is to be noted that a physical system cannot be realized when the gap is close to or

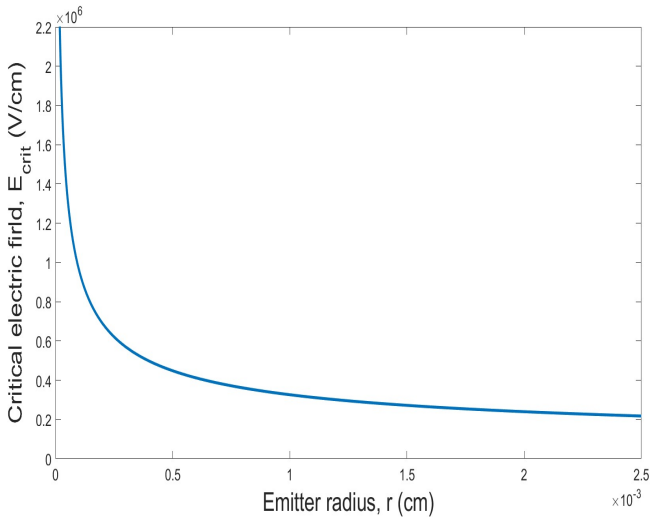

Figure 3.3: Critical electric field at emitter tip as a function of emitter radius based on Peek's formula.

less than the emitter radius. There needs to be sufficient space for the ionization and drift to take place. The gap has to be far bigger than **r** for the sustained discharge to take place.

(3) E_{crit} vs r

After ionization, the airflow in an EHD blower is caused by the electric field gradient, which pushes the ions towards the collector. Thus, a higher electric field tends to provide higher air flow from the outlet, as shown in multiple works. The Peek's electric field based on equation (3.1) clearly shows the importance of a smaller emitter radius. Figure 3.3 shows that for an extremely small emitter radius, a staggeringly high electric field is achievable.

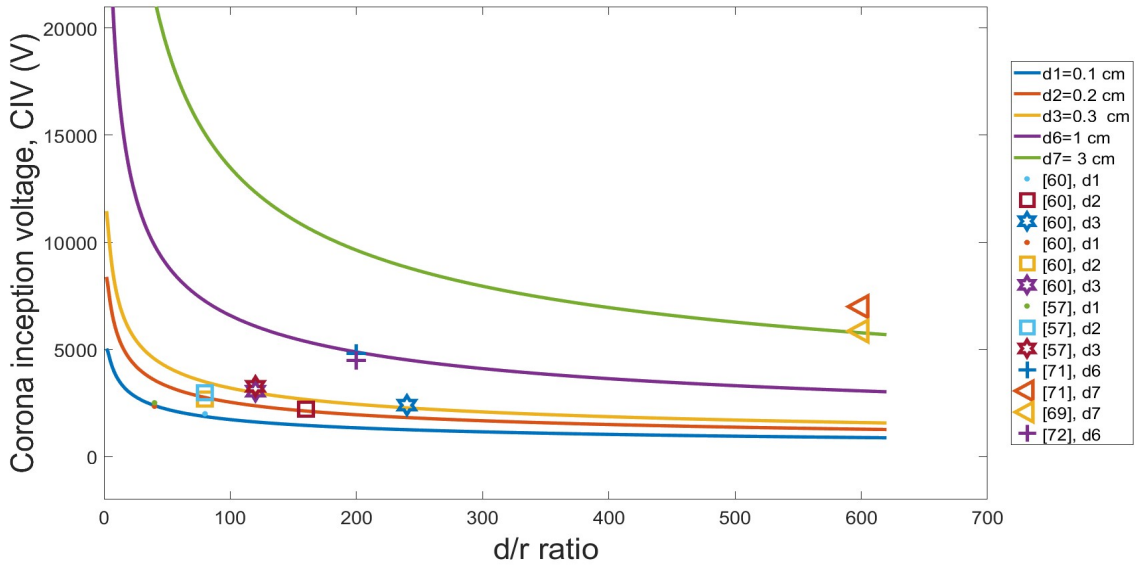

Figure 3.4: CIV as a function of varying d/r ratio for particular interelectrode gaps. Scatter plots from the literature [57, 60, 69, 71, 72] validate the theoretical model.

3.2.2 Impact of the gap-to-radius ratio

Although some papers have previously discussed the impact of both these parameters individually on the system, the impact of the $\boldsymbol{d/r}$ ratio is not thoroughly explained in the literature.

Figure 3.4 shows the change in the corona onset voltage based on the $\boldsymbol{d/r}$ ratio for fixed gaps. For a smaller $\boldsymbol{d/r}$ ratio, the CIV changes sharply compared to a higher $\boldsymbol{d/r}$ ratio. It indicates that for a particular inter-electrode gap, there exists a range of emitter radius for which the CIV changes rapidly, whereas, for extremely high $\boldsymbol{d/r}$, the CIV reduces at a sluggish rate. The graph gives a great visual understanding of the extent of miniaturization needed for the emitter tip to design an efficient EHD system.

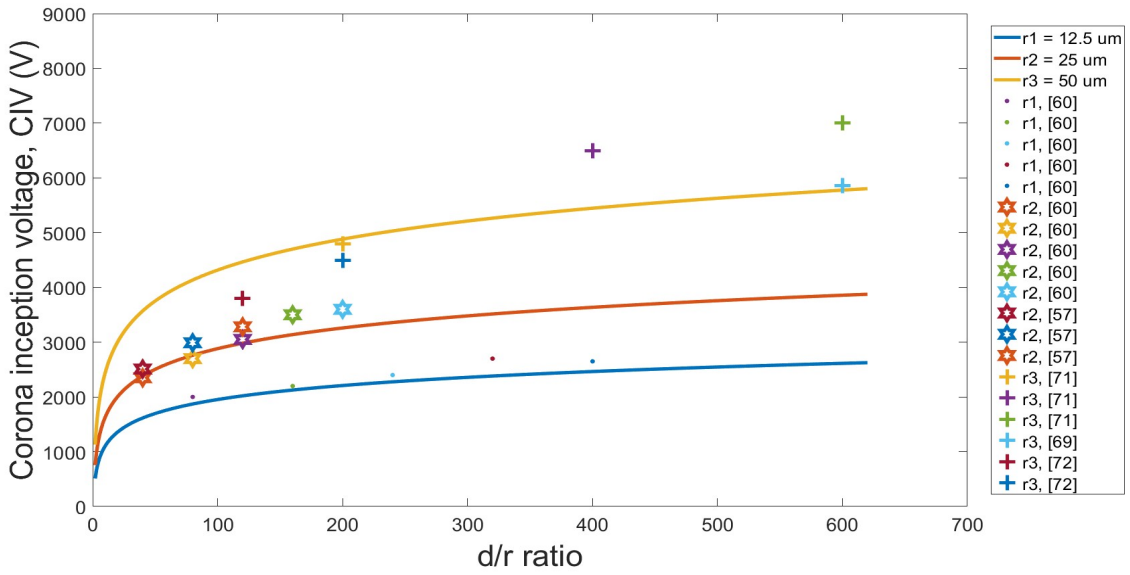

Figure 3.5: CIV as a function of varying d/r ratio for particular emitter tips. Scatter plots from the literature [57, 60, 69, 71, 72] validate the theoretical model.

In Figure 3.5, we see the impact of the $\boldsymbol{d/r}$ ratio on the inception voltage for different emitter tip radii. A clear transition from the rapid increment region to the saturation region can be observed. For a small emitter radius, a small $\boldsymbol{d/r}$ ratio might be needed, indicating the need for a smaller inter-electrode gap in reducing the CIV. Thus, looking into the $\boldsymbol{d/r}$ ratio gives better insight into the design choices.

3.3 FEA modeling

A Finite Element Analysis (FEA) model has been developed using COMSOL Multiphysics to model the ion thrusters or EHD (Electrohydrodynamics) blowers. The results obtained

for CIV and air velocity using similar models previously showed somewhat good agreement with the experimental results [48, 73, 74]. Figure 3.6 shows the geometry used for FEA analysis. The 2D geometry consists of an emitter wire and a collector grid. The diameter of the collector grid wire is 0.1 mm, and the pitch between the wires is 0.5 mm. There is one inlet and one outlet, as defined in Figure 3.6. The entire medium is air, and the walls have been considered conductive [48]. The emitter radius and inter-electrode gaps have been varied, as shown in Table 3.2.

3.3.1 CIV prediction

The electrostatics module can be used to calculate the electric field in the system. We are concerned about the maximum electric field at the emitter tip (E_e). The electric field created at the surface of the emitter (E_{crit}) for a positive corona system can also be found out from Peek's empirical formula (equation (3.1)).

The electric field is obviously directly proportional to the applied voltage. The inherent idea is to increase the voltage to a point where the field E_e becomes equal to the Peek's critical field E_{crit} or E_{peek} for that particular emitter radius. This voltage, where the electric field $E_e = E_{peek}$, can be considered as the CIV. The simulated CIV results have previously shown a good match with the analytical (equation (3.3)) and experimental results.

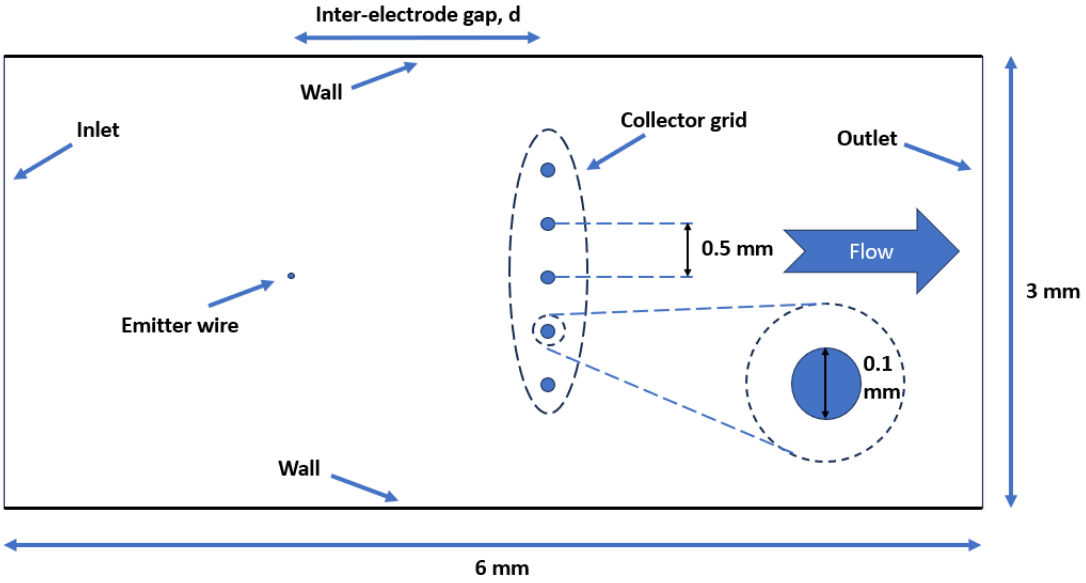

Figure 3.6: 2D wire-to-grid architecture geometry used for FEA analysis (figure not to scale).

3.3.2 Air velocity prediction

For the model to simulate the air velocity, the electrostatics module must be appropriately coupled with the transport of diluted species (tds) and laminar flow modules. Figure 3.7 shows a detailed flowchart of the COMSOL model.

One critical aspect here is to accurately find out the space charge density (SCD) caused due to the discharge process, which can be modeled by coupling the electrostatics and charge transport boundary conditions. A common method to determine the SCD is by implementing Kaptsov's approximation [75]. As per this approximation, the electric field on the emitter surface keeps on increasing as the applied voltage increases but stays constant once the corona is initiated. This means when the applied voltage is equal to or more than the CIV,

the electric field at the emitter surface can be considered to be the same as Peek's critical electric field. Solving for this condition, while the electrostatics and charge transport physics are coupled together, gives us the desired space charge density.

Once the SCD is solved, the laminar flow is coupled with the 'electrostatic' module and the 'transport of diluted species' module to simulate the airflow from the blower, as explained in the flow chart in Figure 3.7.

The following are the equations related to EHD used in our model [48, 76]:

The supply voltage V is dictated by Poisson's equation as,

$$\nabla^2 V = -\frac{\rho}{\varepsilon_0}, \tag{3.5}$$

where ρ is the space charge density (in C/m^3) and ε_0 is the dielectric permittivity of free space (in F/m). The electric field E can be obtained from equation (3.6),

$$E = -\nabla \mathrm{V}. \tag{3.6}$$

The electric current is the result of three effects, as shown in equation (3.7). The conduction is the movement of ions due to the electric field in the system. The convection term depends directly on the airflow as is the transport of charges due to the flow. The last term is related to the charge diffusion. The current density J can be written as,

$$J = \mu_E E\rho + U\rho - D_c \nabla \rho, \tag{3.7}$$

where μ_E is the ion mobility coefficient (in $m^2/V.s$), U is the airflow velocity (in m/s), and D_c is the charge diffusion coefficient (in m^2/s).

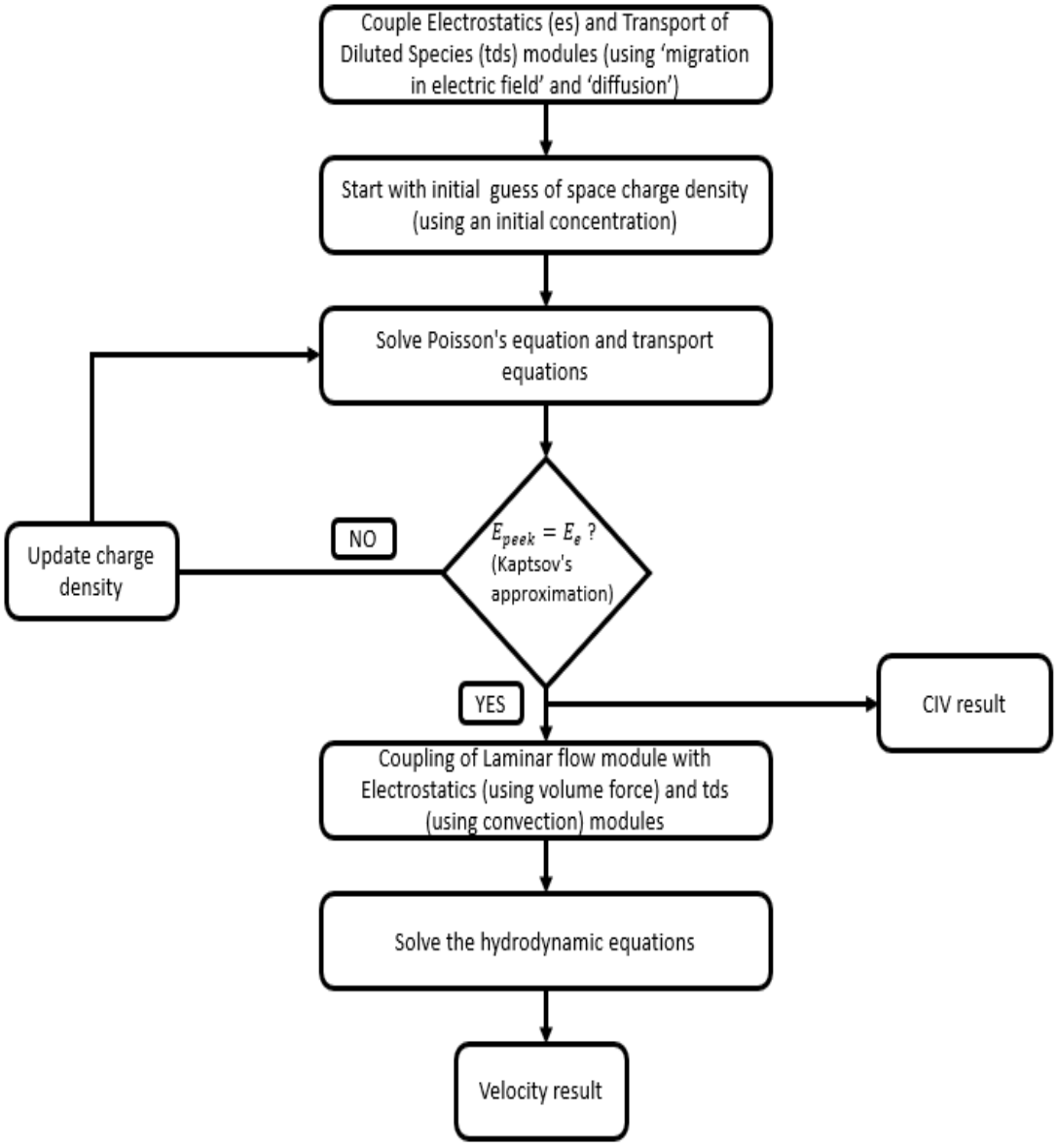

Figure 3.7: COMSOL model flowchart.

The current continuity equation and mass conservation equation are shown in equation (3.8) and equation (3.9), respectively:

$$\nabla.J \ = \ 0, \tag{3.8}$$

$$\nabla.U = \ 0. \tag{3.9}$$

Combining equations (3.7, 3.8, 3.9), we can derive the charge transport equation:

$$\nabla.J = \nabla.\left(\mu_E E\rho - D_c\nabla\rho\ \right) + U.\nabla\rho = 0. \tag{3.10}$$

The Navier-Stokes equations, along with the continuity equation (equation (3.9)), dictate the fluid flow part of the model for incompressible airflow,

$$\rho_{air}U.\nabla\mathrm{U} = -\nabla\mathrm{P} + \mu\nabla^2 U + \rho E, \tag{3.11}$$

where ρ_{air} is the density of air (the fluid medium in this case) in kg/m^3, P is the air pressure (in Pa), μ is the dynamic viscosity of air, and ρE is the body force.

Module	Emitter	Collector and channel wall	Channel inlet	Channel outlet
Electrostatics	Electric potential	Ground	Zero charge	Zero charge
Transport of diluted species	Dirichlet condition, $q = q_0$	$q = 0$	Zero diffusion	Zero diffusion
Laminar flow	No slip	No slip	$u = \sqrt{\frac{2P}{\rho}}$, $v = 0$ [76]	$P_{out} = 0$

Table 3.1: Boundary conditions.

In Table 3.1, the boundary conditions have been noted down. In the electrostatics module, the emitter electrode surface is given the power supply, whereas the collector grid and the

channel walls have been grounded. The space charge is applied to the emitter surfaces. For the laminar flow module, the outlet is given a zero pressure boundary condition, whereas the inlet boundary has been derived from Bernoulli's principle, as suggested by [48, 76].

Parameter	Value
Relative permittivity of air (ε_r)	1
Permittivity of free space (ε_0)	8.854×10^{-12} F/m
Air density (ρ_{air})	1.23 kg/m^3
Ion mobility coefficient (μ_E)	1.8×10^{-4} $m^2.V^{-1}.s^{-1}$
Charge diffusion coefficient (D_c)	5.3×10^{-5} m^2/s
Dynamic viscosity of air (μ)	1.8×10^{-5} $N.s/m^2$
Emitter radius (μm)	0.25-1
Inter-electrode gap (mm)	0.25-1.25
Temperature	293.15[K]
Supply voltage	1500 V

Table 3.2: COMSOL model parameters.

Table 3.2 indicates the key FEA model parameters. The emitter tip radius is varied from 250 nm to 1 μm and the electrode gap is varied from 0.25 mm to 1.25 mm. All designs are simulated at the same voltage of 1500 V.

3.4 FEA results and analysis

This section discusses the results of the designs mentioned above. The focus is on the outlet average air velocity and the CIV.

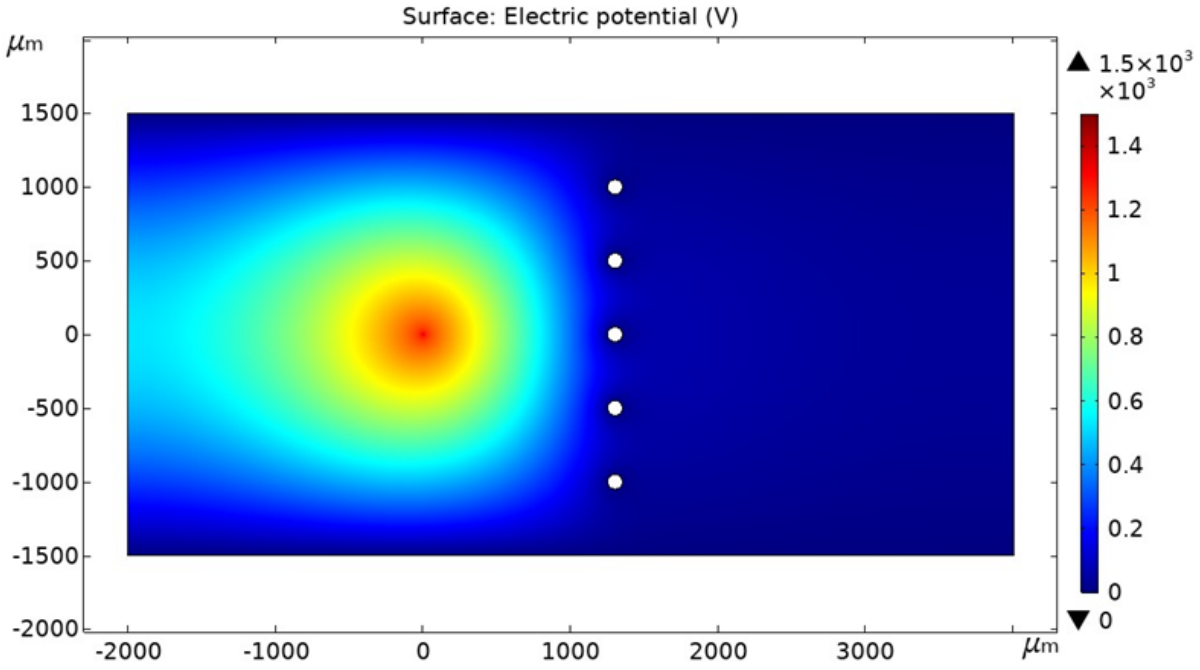

(a)

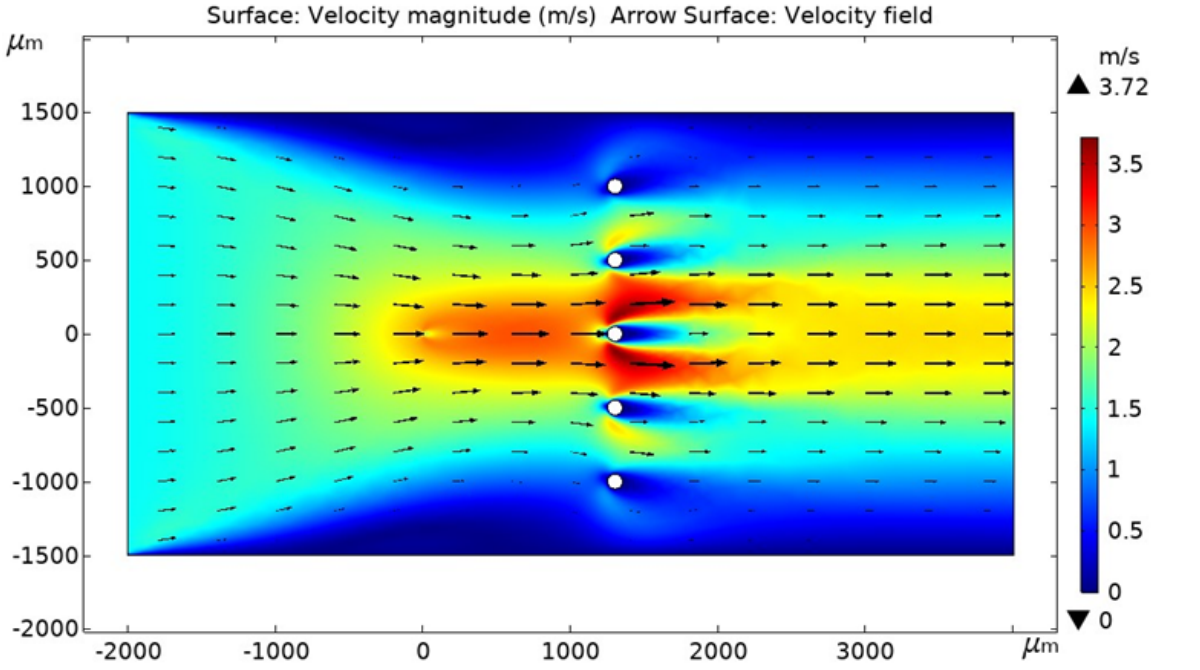

(b)

Figure 3.8: FEA simulation results of (a) potential distribution and (b) air velocity from the outlet for emitter radius 250 nm and inter-electrode gap 1.25 mm.

3.4.1 Simulation plots

Figure 3.8 shows the potential distribution and the air velocity plots. The coronating wire surface has the highest potential, i.e., 1500 V, and the collector grid and channel have zero potential. In Figure 3.8 (b), the arrows show the direction of airflow with the highest outlet air velocity at the center of the outlet.

3.4.2 Air velocity characterization

In this section, the average air velocity at the outlet for each design has been investigated. Figure 3.9 (a) clearly shows that for a fixed emitter radius ($\boldsymbol{r}$), the air velocity decreases dramatically as the inter-electrode gap increases.

Figure 3.9 (b) indicates that the air velocity is inversely proportional to the emitter radius, $\boldsymbol{r}$. Both these plots give us a notion that a smaller inter-electrode gap ($\boldsymbol{d}$) and emitter radius ($\boldsymbol{r}$) tend to yield maximum airflow.

Although a good design approach, in general, should be to reduce the emitter tip radius and electrode gap, there is more to the story. In Figure 3.10 (a), we see how the air velocity changes based on the change in the $\boldsymbol{d/r}$ ratio for a fixed inter-electrode gap. The plot shows an optimal point or at least shows the end of the rapid increment region for a certain gap.

Figure 3.10 (b) clearly shows that for a higher emitter radius, the average air velocity changes rapidly with the $\boldsymbol{d/r}$ ratio. The $\boldsymbol{d/r}$ design choices are more relaxed for smaller emitter radii where the air velocity saturates after a certain $\boldsymbol{d/r}$ ratio.

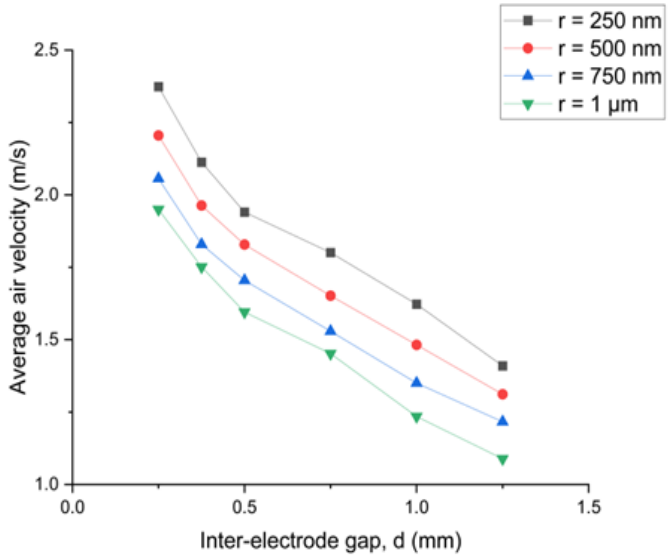

(a)

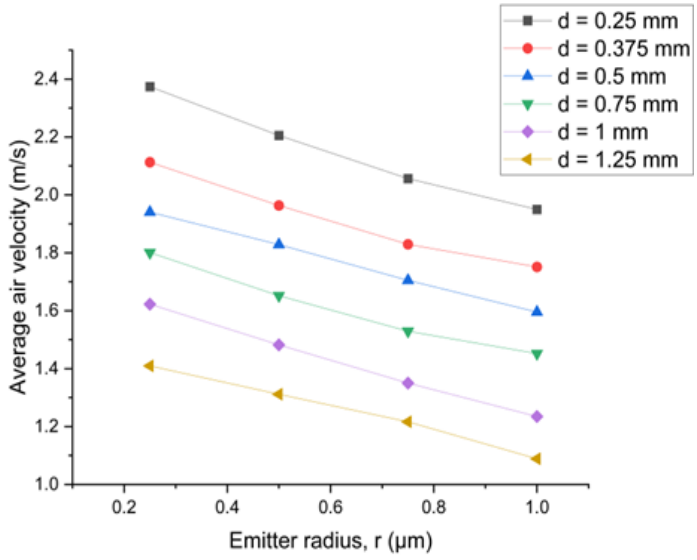

(b)

Figure 3.9: Impact of the inter-electrode gap (***d***) and the emitter radius (***r***) on air velocity.

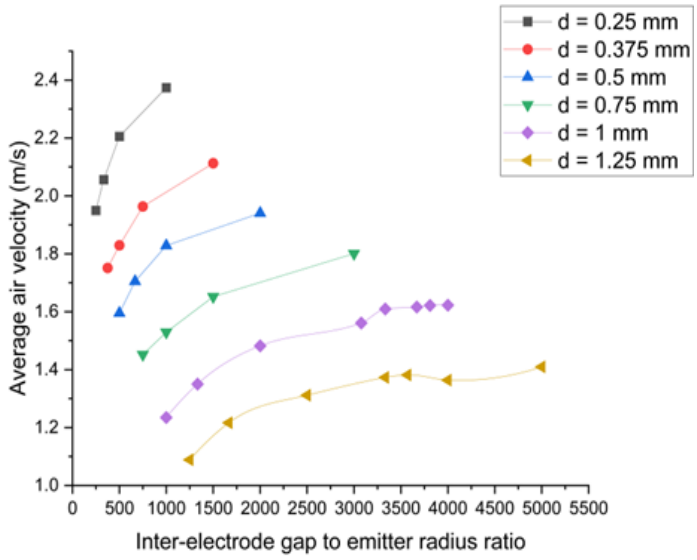

(a)

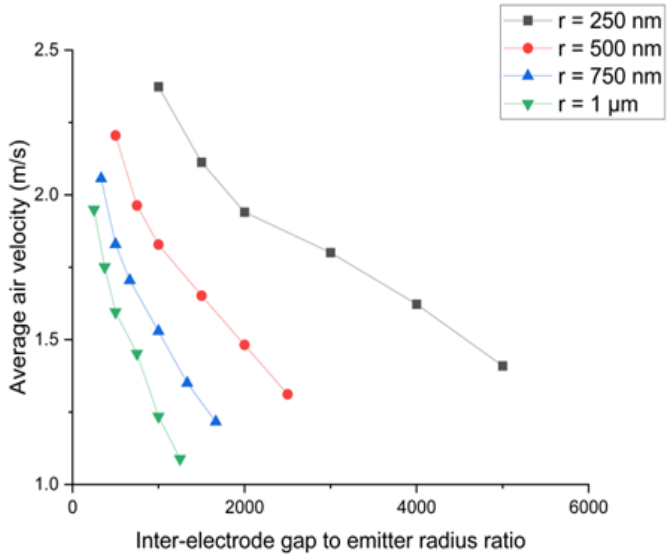

(b)

Figure 3.10: Impact of the inter-electrode gap (***d***) to emitter radius (***r***) ratio (the ***d/r*** ratio) on air velocity.

3.4.3 CIV characterization

The relationship between the CIV and the electrode gap is shown in Figure 3.11 (a). As expected, the inception voltage increases as the inter-electrode gap increases. The FEA simulation results strictly remain within 10% of the analytical solution governed by equation (3.3).

Figure 3.11 (b) shows an almost linear increment in the inception voltage with respect to increasing emitter radius for a fixed gap. We previously talked about the linear region of operation for a small inter-electrode gap in section 3.2, and this is exactly what we observe here.

Figure 3.12 shows the impact of the $\boldsymbol{d/r}$ ratio on the CIV, and the trend matches with our previous literature analysis.

3.5 Discussion and insights

As we now understand the impact of the $\boldsymbol{d}$, $\boldsymbol{r}$ & $\boldsymbol{d/r}$ ratio, we can further discuss its potential impact on propulsion and cooling applications.

The solid-state propulsion has no moving part, resulting in almost silent operation without producing harmful combustion emissions. Such propulsion application has two key important metrics: (a) the thrust-to-weight ratio and (b) the thrust-to-power ratio or thrust efficiency, defined by:

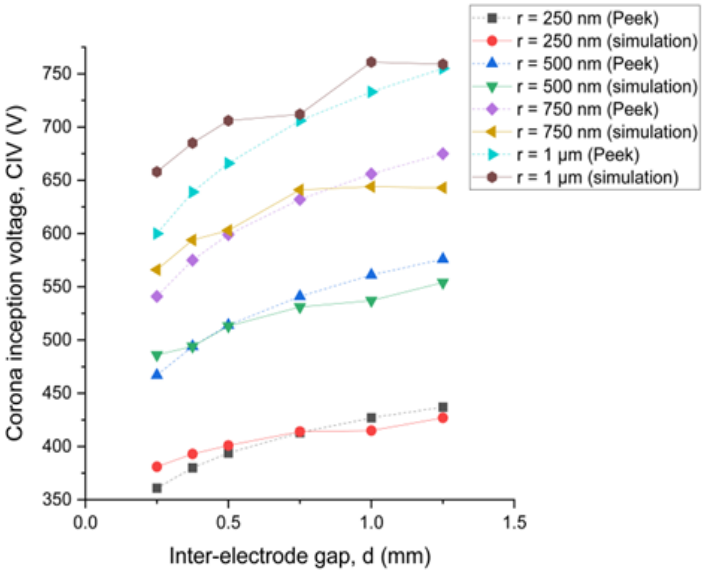

(a)

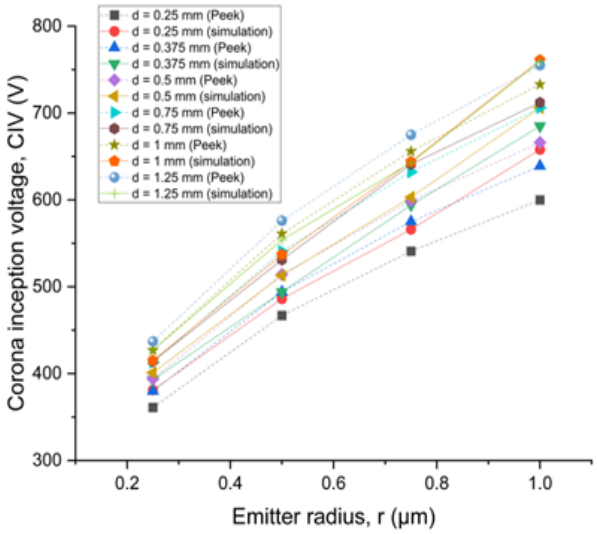

(b)

Figure 3.11: Impact of the inter-electrode gap (***d***) and the emitter radius (***r***) on corona inception voltage (CIV).

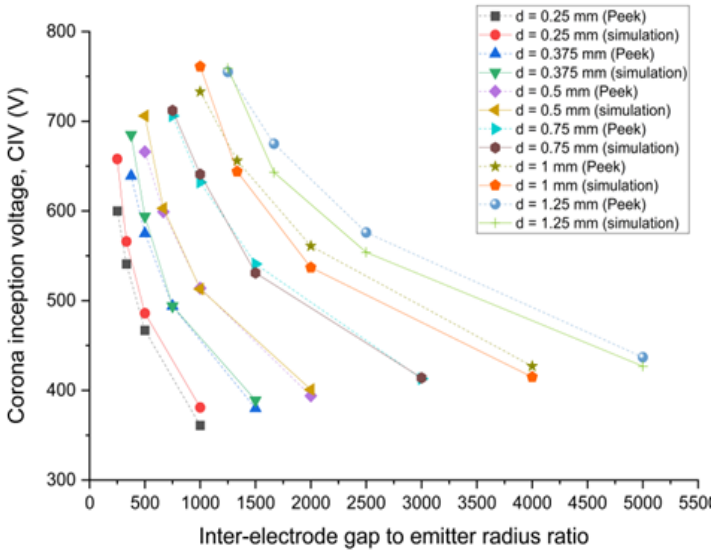

(a)

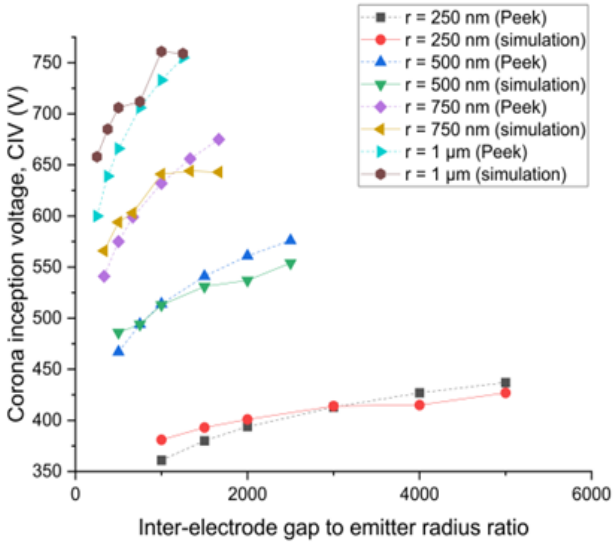

(b)

Figure 3.12: Impact of the inter-electrode gap (***d***) to the emitter radius (***r***) ratio (the ***d/r*** ratio) on corona inception voltage (CIV).

$$Thrust - to - weight \quad ratio = \frac{thrust \quad produced}{device \quad weight} \tag{3.12}$$

$$Thrust - to - power \quad ratio = \frac{thrust \quad produced}{Power \quad consumed} \tag{3.13}$$

A miniaturized ionocraft, because of its extremely low weight, tends to provide a higher thrust-to-weight ratio. Miniaturization also reduces the consumed power, maximizing the overall thrust efficiency. One big challenge for an ion propulsion system is that it requires extremely high voltage. The operational voltage is related to the CIV, as the CIV indicates the minimum range where the device can potentially operate.

The thrust generated from an EHD system can be calculated as [14, 64],

$$F = \frac{Id}{\mu}, \tag{3.14}$$

where μ is the ion mobility coefficient. We know that the power consumption of the system is,

$$P = VI. \tag{3.15}$$

Thus, the thrust-to-power ratio turns out to be,

$$\frac{F}{P} = \frac{d}{V\mu} = \frac{1}{\mu E}. \tag{3.16}$$

The thrust-to-power ratio directly depends on the electric field intensity which can be controlled. Equation (3.14) can further be expanded using Townsend's equation as,

$$F = CV(V - V_{crit})\frac{d}{\mu}. \tag{3.17}$$

Equation (3.17) suggests that, in order to increase the thrust, the geometrical constant

'C' should be maximized, whereas the CIV should be minimized. Since the value of the latter scales down with size, the miniaturization of the EHD device becomes a more exciting prospect to investigate. Equation (3.16) and equation (3.17) show that there is a tradeoff between the thrust and the thrust-to-power ratio, a design sacrifice to be made for propulsion applications.

An EHD blower converts electrical energy to mechanical energy. Thus, the electromechanical energy conversion efficiency can be written as,

$$\eta = \frac{Power_{out}}{Power_{in}} = \frac{P_{mechanical}}{P_{electrical}} \tag{3.18}$$

or,

$$\eta = \frac{1}{2}\frac{A\rho_{air}U^3}{VI}, \tag{3.19}$$

where ρ_{air} is the density of the fluid, A is the outlet cross-section of the device, and U is the outlet air velocity.

Another way of measuring the efficiency of a solid-state fan is the volume of air it removes per unit of power consumed, called the transduction efficiency.

$$Transduction \quad efficiency = \frac{flow \quad (in \quad CFM)}{Power \quad (in \quad Watt)} \tag{3.20}$$

Miniaturization looks attractive as it might result in smaller voltage, current, and effectively higher efficiency, given that the device can generate equivalent airflow. In this chapter, we already explained in detail that devices with a small emitter radius and inter-electrode gap can generate high air velocity.

The research shows that the emitter radius and inter-electrode gap, which often relates to the overall size of the system, have a profound impact on performance. The inter-electrode gap has a huge impact on the airflow, whereas the emitter radius has a major impact on the CIV. The miniaturization of EHD devices seems a logical step ahead, which can be achieved using traditional microfabrication, aiming to reach sub-micron emitter features. Both the emitter radius and the inter-electrode gap at a small scale can become extremely complex to fabricate. The $\boldsymbol{d/r}$ ratio can be extremely helpful in this regard to choose achievable '$\boldsymbol{d}$' and '$\boldsymbol{r}$' without significantly sacrificing the performances.

Having said that, the numerical model should be a guide to designing ion thrusters but should not be used for strict quantitative prediction. We expect the trends to follow, albeit the quantitative results might vary quite a bit. This is especially important for experimental works with unique and unexplored geometries.

Chapter 4

Device Architectures & Characterization

In this section, two novel ion thruster designs have been experimentally examined. Design 1 deals with a single-emitter needle-to-ring architecture where a probe needle is used as an emitter. In design 2, a die-level implementation is shown. In this multi-emitter architecture, multiple microwires are used as emitters.

4.1 Design 1: Probe needle architecture

The probe needle architecture uses a single probe needle as an emitter. The idea is to have separate device building blocks that can be assembled together to build the complete miniaturized EHD blower. The following section talks about the assembly technique.

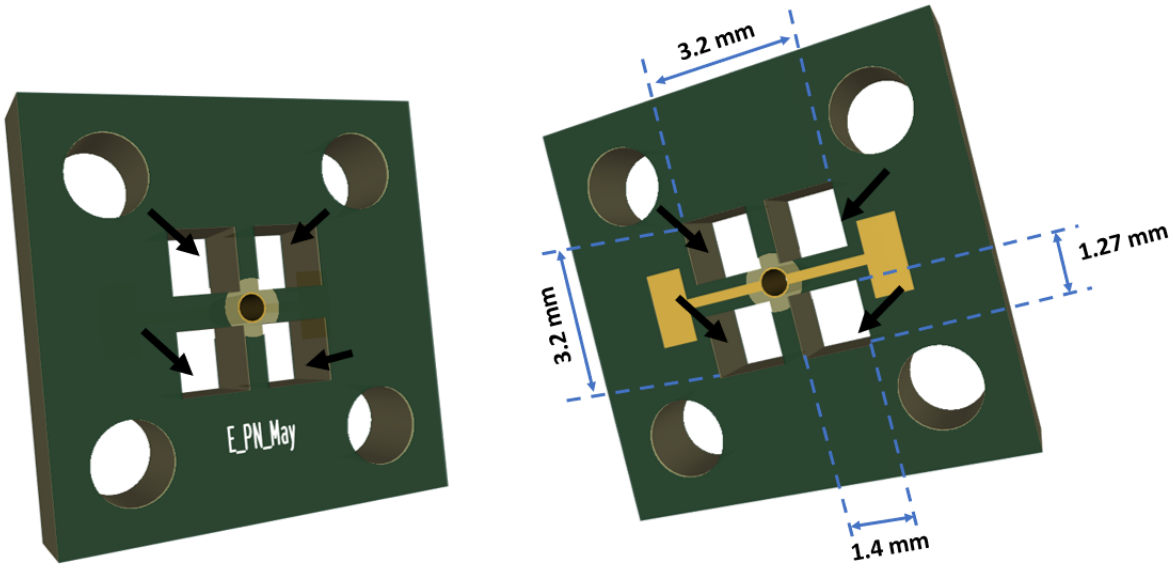

Figure 4.1: Emitter PCB: Front and backside (with metal pads) are shown, and inlet holes are shown with black arrows.

4.1.1 Assembly technique

The assembly requires three fundamental building blocks:

(a) Emitter PCB:

The emitter printed circuit board (PCB) is the block that houses the probe needle. It consists of a hollow via at the center, which connects with pads on the other side for connection. As depicted in Figure 4.1, there are 4 inlet holes with the same dimension of 1.4 mm $\times$ 1.27 mm. The PCB also has 4 holes at 4 corners to accommodate screw holes. A probe needle made of dumet (copper clad iron) is inserted through the via and soldered from the back. The extended needle can then be cut.

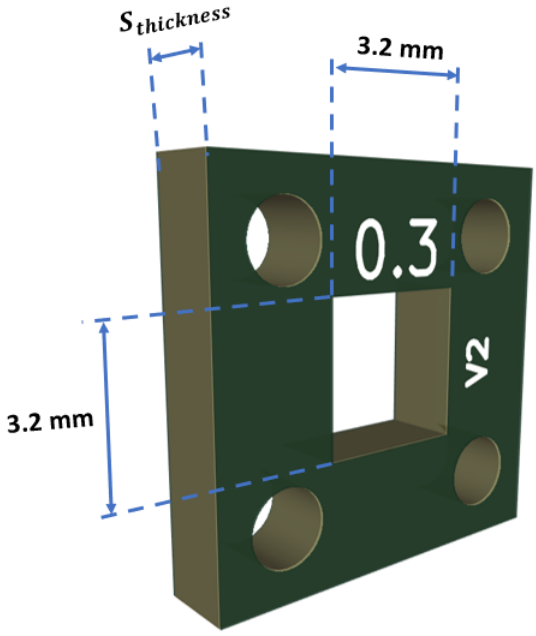

Figure 4.2: Spacer PCB with dimensions.

(b) Spacer:

The spacer is made of bare FR4 PCBs, which separate the emitter and collector PCB electrically. The spacer has a 3.2 mm × 3.2 mm cutout in the middle, as shown in Figure 4.2, which creates a confined air gap between the electrodes. The thickness of the spacer PCB ($S_{thickness}$) dictates the inter-electrode gap.

(c) Collector PCB:

The collector PCB also consists of a via at the center. Figure 4.3 shows the front and back sides of the collector PCB. The front side faces the emitter, separated by the spacer. The

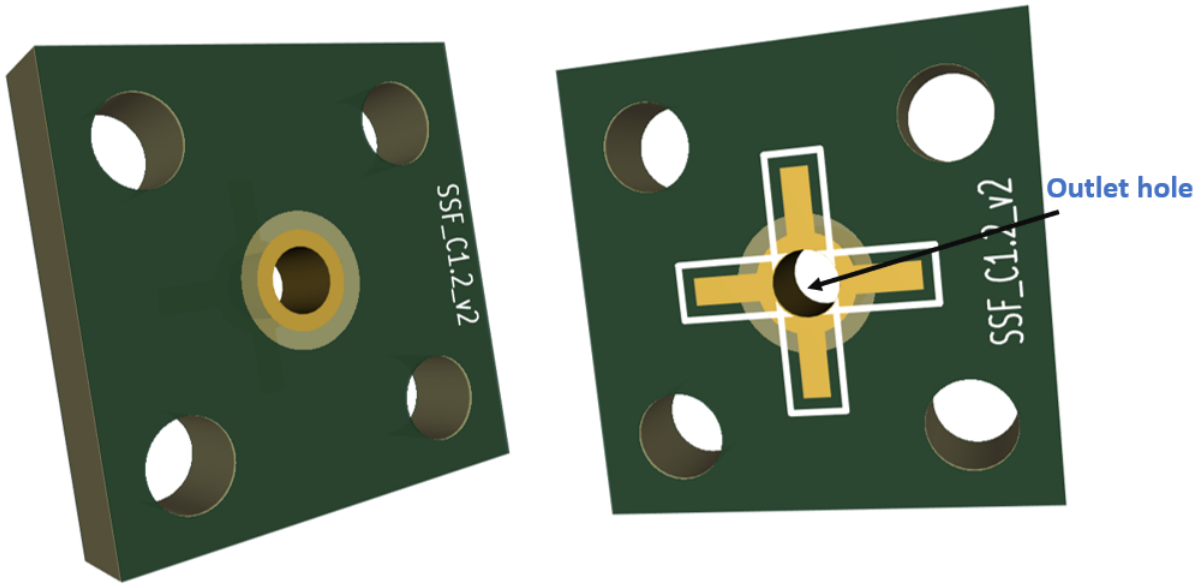

Figure 4.3: Collector PCB: The front side faces the emitter and the back side with the metal pads is visible.

back side metal pads are there for the power supply connection. The diameter of the via can be tuned, resulting in a controllable outlet size. A 1.2 mm diameter via was used in this experiment.

All 3 building blocks have the same dimension of 8.3 mm × 8.3 mm and host 4 screw holes at the 4 corners. These three building blocks can be assembled together using screws and nuts. The thickness of the emitter and collector PCBs are kept at 1 mm, although this shouldn't be a key parameter of concern. The same size and the screw hole positions facilitate alignment and the creation of a confined channel. Figure 4.4 shows an assembled device in scale comparison to a Canadian quarter dollar coin. The assembly thus creates a

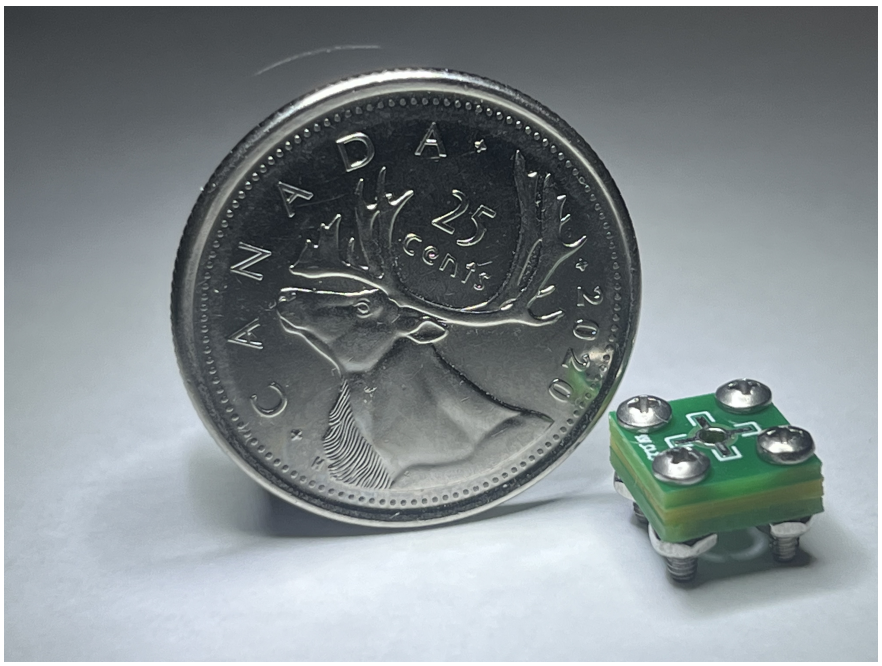

(a)

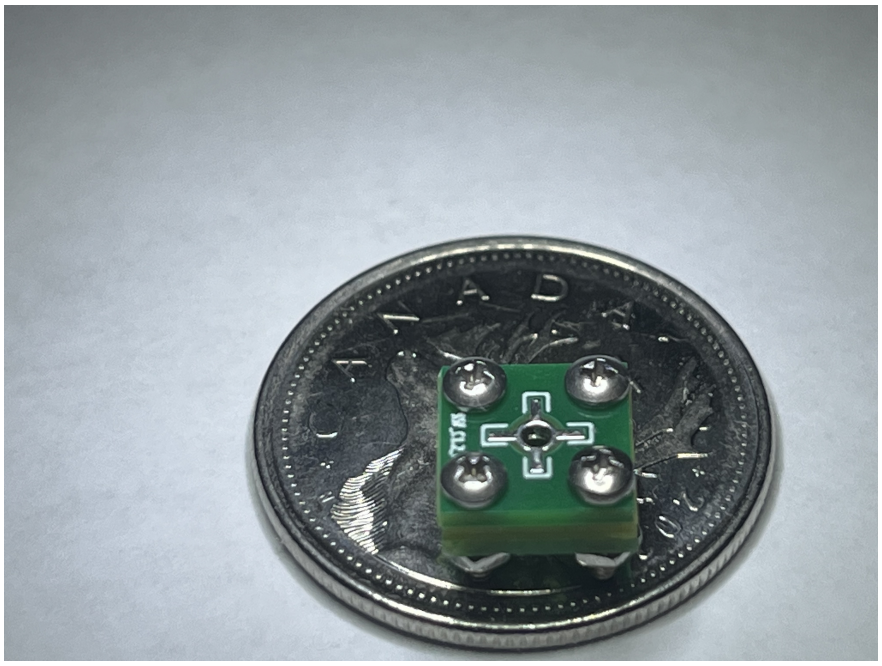

(b)

Figure 4.4: Assembled design 1 device (based on the probe needle architecture), with a Canadian quarter (for reference, a US quarter dollar is $\sim$ 1.6% larger than a Canadian quarter dollar in diameter [77, 78]).

needle-to-ring architecture.

The assembly technique offers extreme customizability. The spacer thickness can be changed, resulting in variable inter-electrode gaps without changing anything else in the overall design. There are defined inlets, outlets, and a closed channel, unlike most setups in the literature. All parameters, such as the inlet hole size, outlet size, channel width, etc., can be tuned by modifying the PCB designs.

4.1.2 Experimental setup

Figure 4.5 presents the schematic of the laboratory setup used to gather the experimental data. The high voltage is provided to the device using a tunable HVPS (high voltage power supply), as shown. The ammeter is connected between the collector side and the ground to measure the discharge current. A high-precision hot wire anemometer (KIMO VT 100) was used to measure the outlet air velocity. As the size of the inlet of the anemometer is larger than that of the outlet size, the anemometer is expected to experience the full outlet airflow, eliminating the need to record measurements at different points. The same approximation was adopted in [58].

It has already been discussed that smaller '$\boldsymbol{d}$' and '$\boldsymbol{r}$' are extremely important in low-voltage ion thruster designs. In this context, investigation of the sub-millimeter inter-electrode gap ion thruster is of utmost interest. There is only a single experimental work by Tirumala that discussed the impact of varying sub-millimeter gaps on the CIV

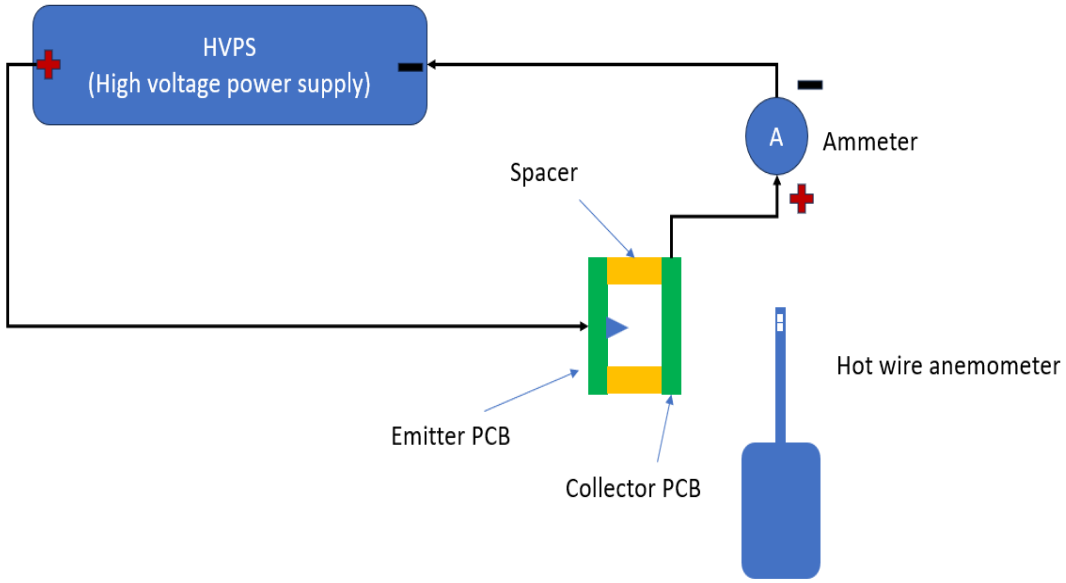

Figure 4.5: Experimental setup schematic for the probe needle architecture.

[60]. In our setup, the assembly process facilitates achieving sub-millimeter inter-electrode gaps with confined channels without the need for any cleanroom facilities. We have investigated the system performance (i.e., the outlet air velocity and CIV) for two different inter-electrode gaps: (a) Case 1 ($d = 0.2$ mm) and (b) Case 2 ($d = 0.8$ mm).

4.1.3 V-I Characteristics

Figure 4.6 shows the V-I relationship for 2 inter-electrode gaps. The microammeter shows no detectable discharge current, until a certain voltage when a small current becomes detectable. This voltage indicates the onset of the corona or the CIV. As the voltage is further increased, the current increases exponentially.

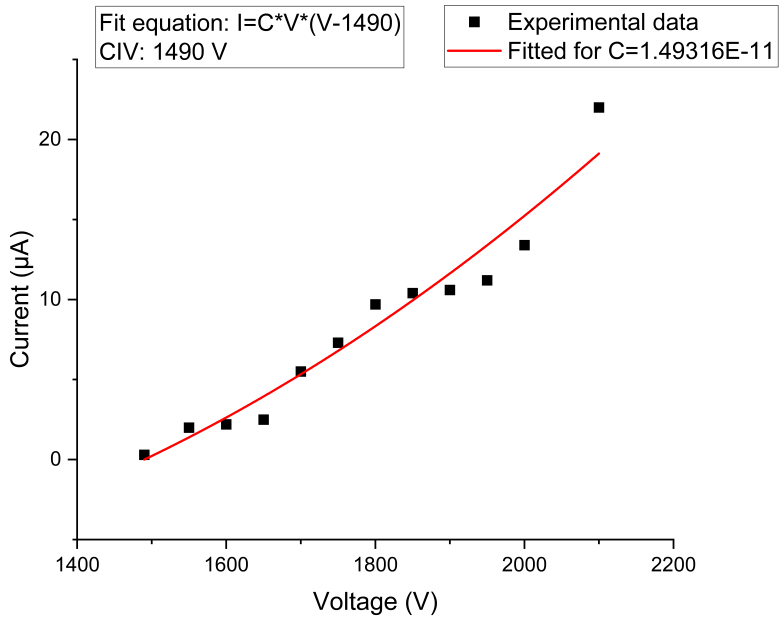

(a)

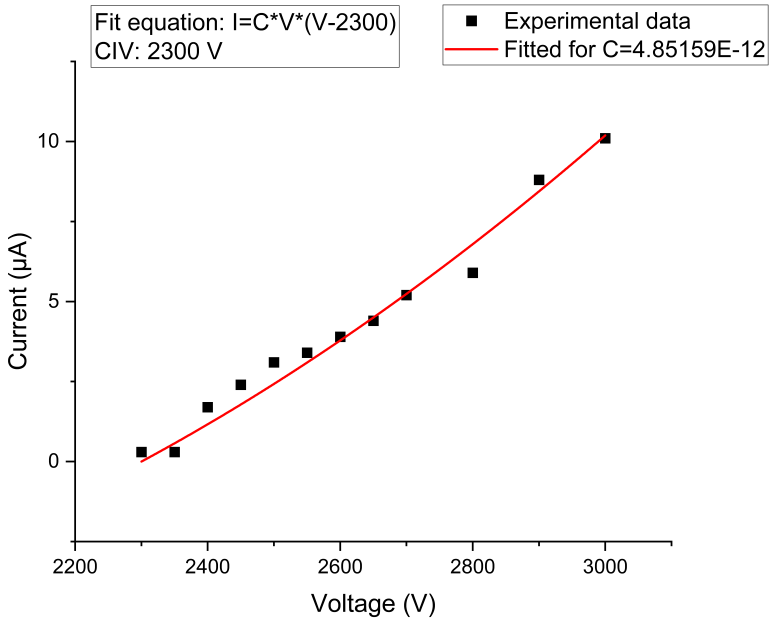

(b)

Figure 4.6: Best fitted '$\boldsymbol{C}$' in Townsend's equation (equation (3.4)) (a) for Case 1 ($d = 0.2$ mm) & (b) for Case 2 ($d = 0.8$ mm). The unit of '$\boldsymbol{C}$' is in A/V^2.

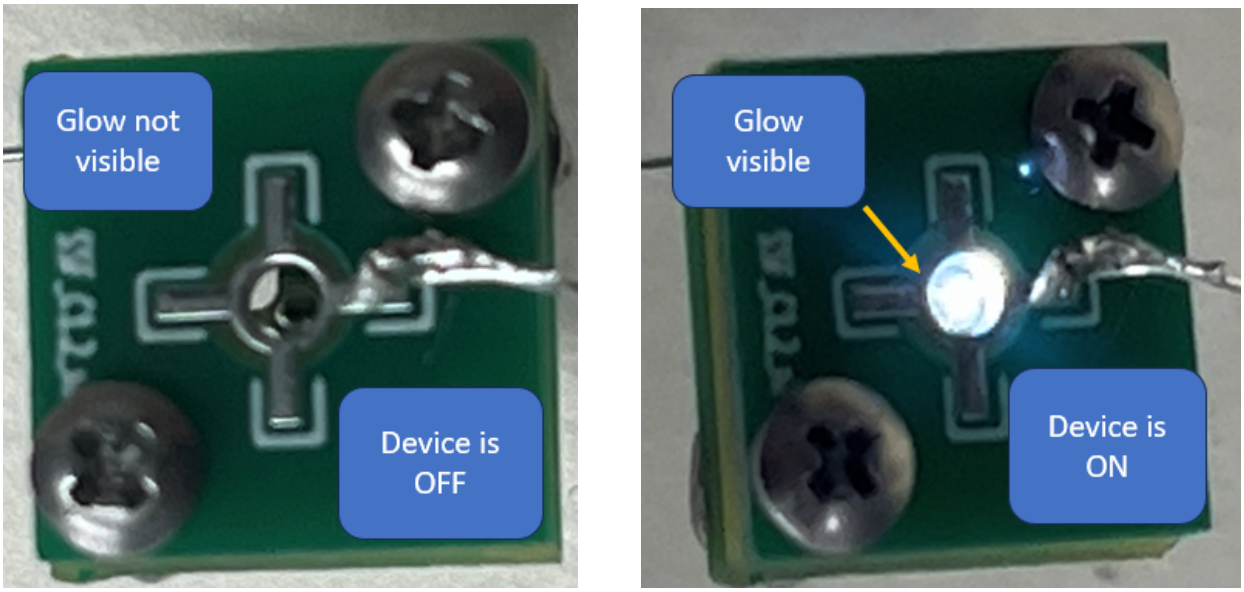

(a) **(b)**

Figure 4.7: (a) Device at OFF state (no corona discharge), (b) Device in action: The glow generated by the corona discharge is visible from the outlet of the device.

The geometrical coefficient '$\boldsymbol{C}$' is an important parameter which, in general, should be maximized. Figure 4.6 also shows the fitted '$\boldsymbol{C}$' for both gaps as per Townsend's equation (equation (3.4)). A higher '$\boldsymbol{C}$' of $\sim 1.49 \times 10^{-11}$ A/V^2 was achieved for Case 1 ($d = 0.2$ mm). A higher '$\boldsymbol{C}$' for a smaller gap is expected and the same has been achieved in the experiment.

We already know that a smaller gap results in a lower CIV, and the experimental data matches the expectations. For Case 1 ($d = 0.2$ mm) the CIV is 1490 V, and for Case 2 ($d = 0.8$ mm) the CIV is 2300 V.

Figure 4.7 also shows the device when it is idle and while it is operational. When supplied

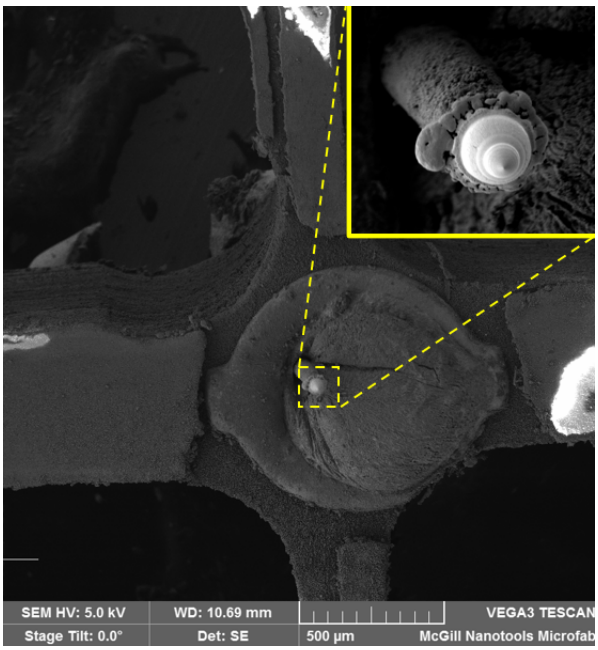

Figure 4.8: SEM photo of the device probe needle after operation. The inset shows the zoomed emitter tip and the needle surface morphology.

with sufficient voltage (more than the CIV), a visible glow was observed, which indicates the plasma generation.

The SEM image of the needle after the operation is shown in Figure 4.8. Generally, the morphology of an emitter surface changes after operation. More about this has been explained in Section 6.2.1. The inset shows that the tip diameter is $\sim 45\ \mu m$ and the point radius is $\sim 0.35\ \mu m$.

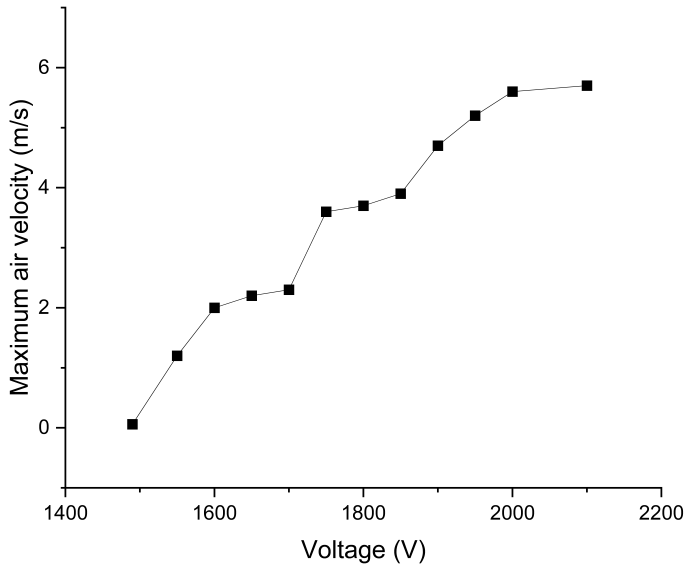

(a)

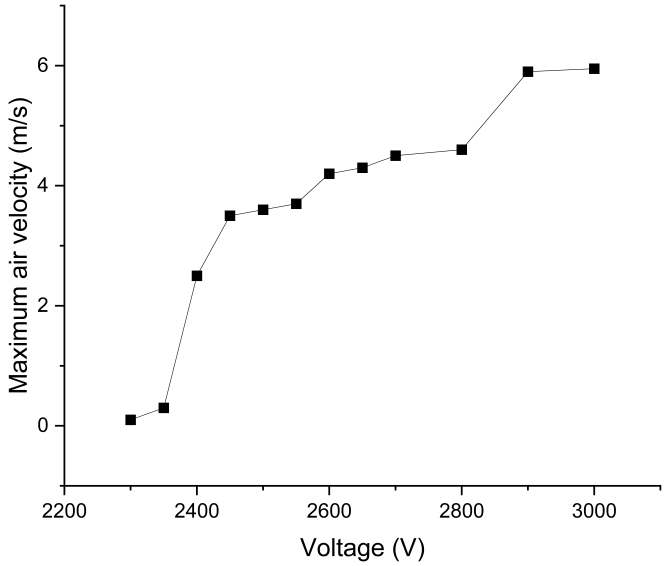

(b)

Figure 4.9: Maximum air velocity as a function of the supply voltage achieved experimentally for (a) Case 1 ($d = 0.2$ mm), and (b) Case 2 ($d = 0.8$ mm).

4.1.4 Air velocity characterization

The primary objective is to find the outlet air velocity for varying inter-electrode gaps. Different gaps have been achieved by controlling the spacer thickness. Figure 4.9 plots the measured air velocity from the outlet for both cases. The air velocity shows an almost linear relationship with the applied voltage, as expected. For Case 1, a maximum air velocity of 5.7 m/s at 2100 V operational voltage was achieved. In Table 4.1, a few ion thruster designs are compared to this work, in terms of the outlet velocity achieved. In Case 2, the maximum air velocity of 5.95 m/s was recorded at 3000 V. ***The wind velocity is one of the highest ever reported at this voltage and scale for a single-stage, single-emitter device***. The airflow can be further increased with multiple emitters or multiple stages.

As per our numerical analysis, for a certain operational voltage (given that it is between the CIV and the breakdown voltage), a smaller inter-electrode gap tends to yield higher wind velocity. The graph matches this expectation. For example, an air velocity of 3.6 m/s was recorded at 2500 V for Case 2, where the inter-electrode gap is 0.8 mm. The same amount of wind velocity was achieved at 1750 V for Case 1 ($d = 0.2$ mm).

4.1.5 Thrust characterization

Thrust can be calculated from the measured air velocity using the mass flow equation:

$$F = mv = \rho_{air} A v^2, \tag{4.1}$$

where ρ_{air} is the air density, A is the outlet cross-sectional area, and v is the outlet air

Work	Maximum air velocity (m/s)	Operational voltage (V)	CIV (V)
[79]	6.3	12000	7000
[80]	1.5	16000	-
[81]	4.5	8000	-
[82]	9	8000	-
[48]	1.9	8000	4060
This work (Case 1)	5.7	2100	1490
This work (Case 2)	5.95	3000	2300

Table 4.1: Comparing the air velocity and CIV for different DC EHD systems.

velocity. Figure 4.10 plots the thrust-to-power ratio as a function of the applied voltage for 2 Cases. After the corona inception, as the voltage increases, the thrust-to-power ratio increases rapidly before it starts to decrease sluggishly. The result is similar to the work shown in [83]. This gives us an indication that an operational voltage near the inception voltage might be a good choice solely from the perspective of achieving high efficiency. From the previous analysis, we already know that a larger gap tends to give higher thrust. In this plot, we see a higher thrust-to-power ratio for a larger inter-electrode gap. The impact of the inter-electrode gap follows a similar trend to several works from the literature focused on large inter-electrode gaps ($>$ 1 cm) [37, 84]. Thus, the expectations remain valid, even for sub-millimeter gaps. A maximum thrust-to-power ratio of 2.9 mN/W was achieved for a 0.8 mm gap at 2450 V.

The thrust density is another key parameter for propulsion (Figure 4.11). It signifies the thrust generated per unit outlet area. Both cases exhibit extremely high thrust density, with Case 2 being the highest with $\sim 43.55\ N/m^2$. As thrust density is directly proportional to

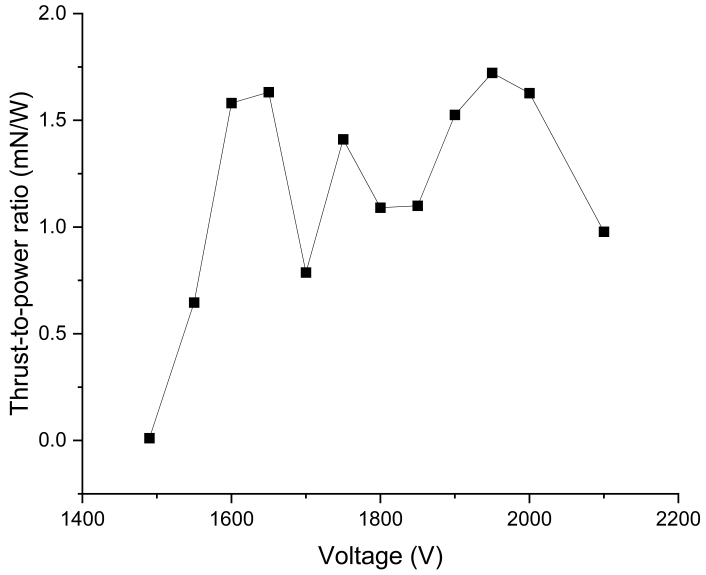

(a)

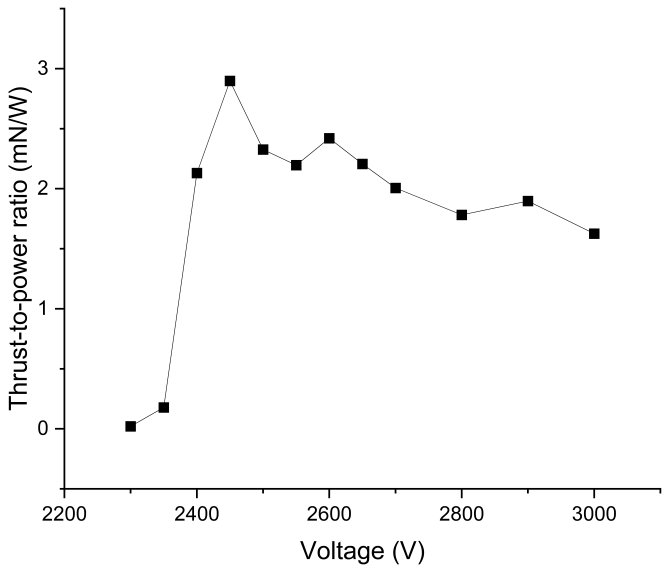

(b)

Figure 4.10: Thrust-to-power ratio as a function of the supply voltage for (a) Case 1 ($d = 0.2$ mm), and (b) Case 2 ($d = 0.8$ mm).

the thrust generated with the outlet area being constant, a higher thrust density for a larger gap was expected. The experimental data thus concords with the expectation.

Table 4.2 documents some ion thrusters with their thrust densities. Both Cases in our work exhibit significant improvements to the previous works in the literature. Important to note that some of the works listed in the table used multiple stages to achieve high thrust density, whereas our design is a single-emitter single-stage device with far less design and assembly complexity. The thrust densities achieved are the highest for any single-stage EHD thruster of this scale ever reported in the literature.

Thrust density and thrust-to-power are two key parameters and there is a tradeoff between them, thus making it futile to look at them in isolation. A scatter plot is presented in Figure 4.12, for better visualization of our designs compared to other miniaturized devices. The plot clearly emphasizes the significance of this work. It is well known that adding multiple stages together can increase the thrust density. The thrust density scales by a factor of $\sqrt{n}$ with the number of stages, as suggested in [85], where '$\boldsymbol{n}$' is the number of active stages. Thus, a high thrust-to-power ratio configuration can be chosen to build a multi-stage ducted (MSD) device in order to achieve optimal thrust-to-power ratio and high thrust density.

Another approach to get a good idea about the efficiency of the device is by checking the thrust density per unit power. In [14], a thrust density per unit power of 151.17 N/m^2W was reported by the authors. In our design, a maximum thrust density per unit power of

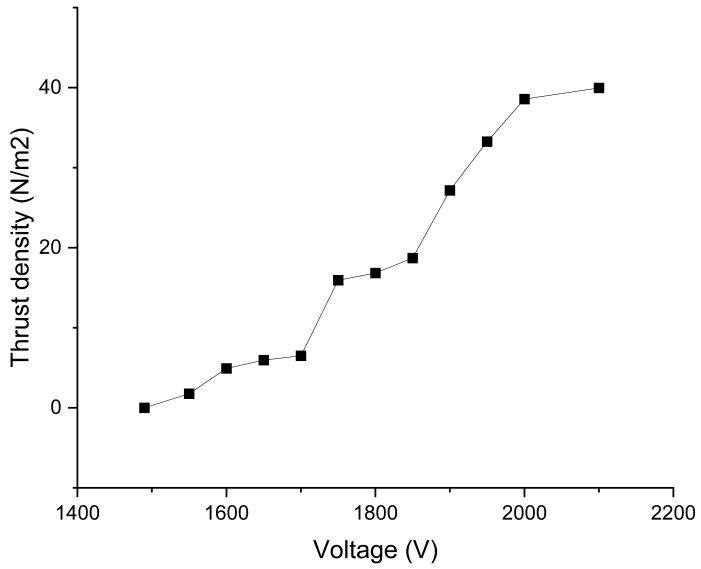

(a)

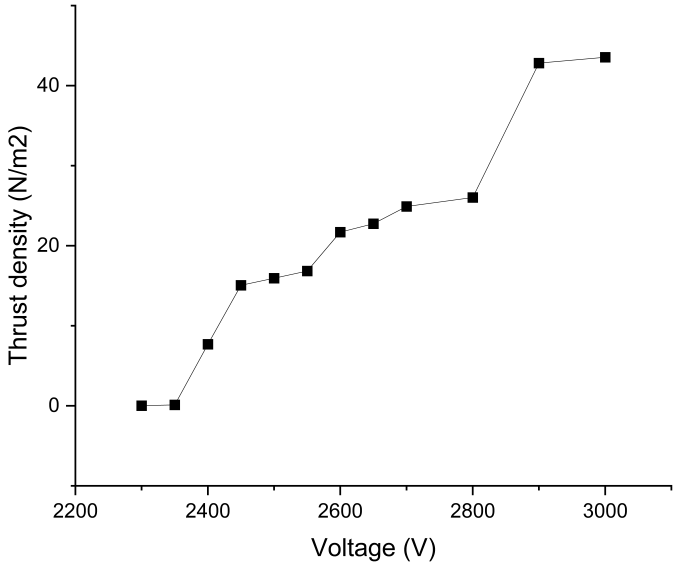

(b)

Figure 4.11: Thrust density as a function of the supply voltage for (a) Case 1 ($d = 0.2$ mm), and (b) Case 2 ($d = 0.8$ mm).

$> 2000\ N/m^2W$ was achieved for Case 2. This extremely high efficiency is due to the high thrust density and low power consumption by the miniaturized device.

Work	Thrust density (N/m^2)
[88]	3.3
[87]	8.7
[14]	13.67
[86]	15
[83]	18
This work (Case 1)	39.96
This work (Case 2)	43.55

Table 4.2: Comparing thrust density for different DC EHD systems.

4.2 Design 2: Microwire architecture

Improvement of an EHD device is possible by following a few design modifications mentioned in the literature, for example, by optimizing the inlet/outlet dimensions, using a covering on the emitter made of insulating material to produce a focused electric field, using multiple emitter stages, etc. [86, 89–93]. Although these changes can slightly improve the velocity/thrust performance, the reduction of the CIV needs more miniaturization.

The need for further miniaturization of EHD systems inevitably leads to microfabrication. The aim is to controllably fabricate devices with a small emitter radius and investigate the impact of multiple-emitter architectures.

In the following section, a novel microfabrication technique is proposed in order to

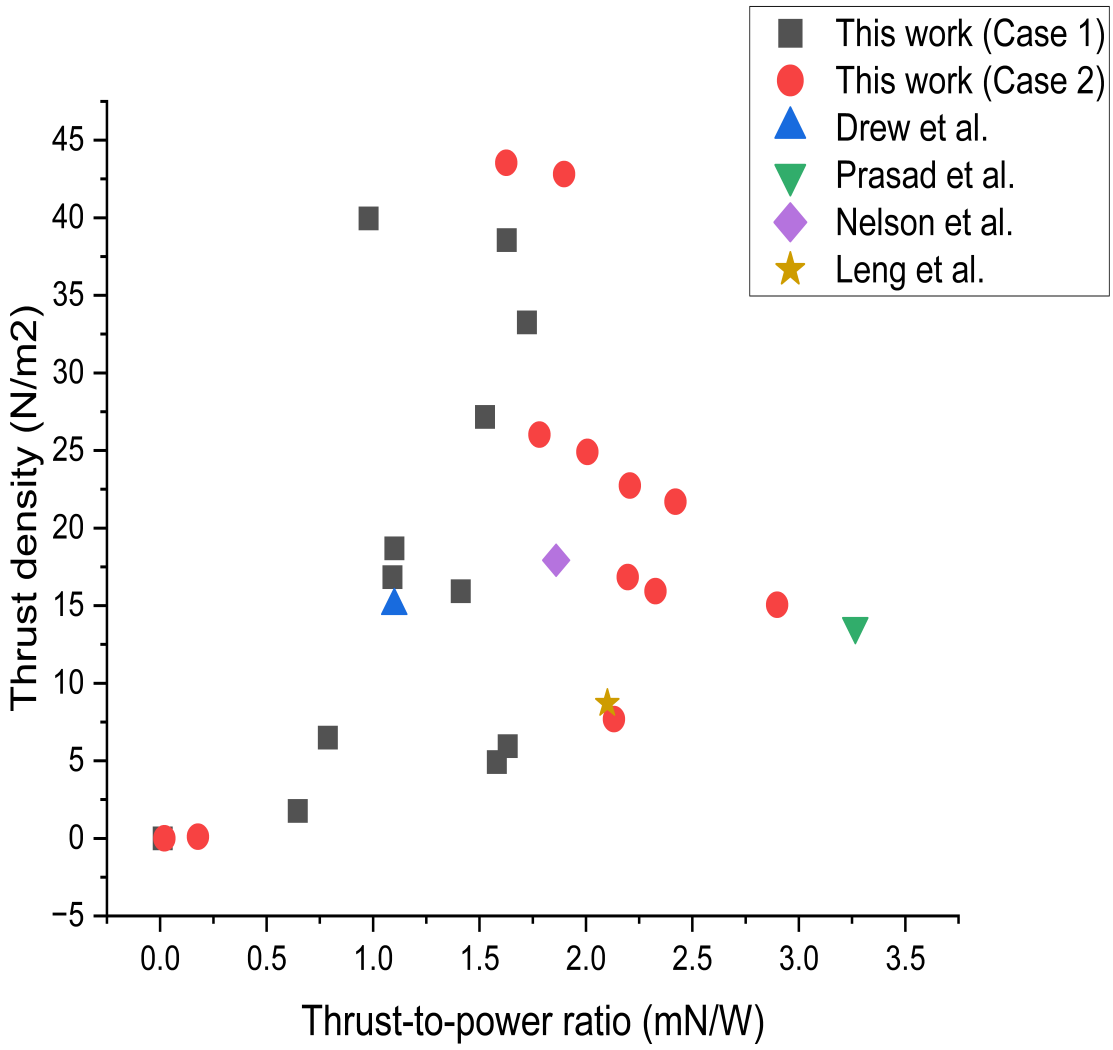

Figure 4.12: Comparing 2 key performance performances (thrust-to-power ratio and thrust density) of miniaturized air medium ion thrusters with Design 1. Four previous works have been used: Drew et al. [86], Prasad et al. [14], Nelson et al. [83], and Leng et al. [87].

fabricate small-diameter silicon microwires. This should result in low voltage sustained corona generation.

4.2.1 Microwire fabrication

The fabrication process to controllably fabricate silicon microwires is shown in Figure 4.13. A p-type silicon wafer with a resistivity of $0.003 - 0.005\ \Omega.cm$ was chosen for the process. After removing the native oxide using HF, the sample was primed with HMDS for 2 minutes. The sample is then spin-coated with approximately 1.6 μm AZ5214 E photoresist, as shown in Figure 4.13 (b). A soft bake at $110°C$ (50 seconds) was performed. After the sample was cooled down, it was exposed to a dose of 55 mJ/cm^2. A post-exposure bake ($120°C$, 2 minutes) reverses the tone of the resist. This step is extremely critical as it dictates the resolution and proper development. Subsequently, the sample was flood-exposed to 250 mJ/cm^2 energy. The development was done using AZ726 MIF. The development creates holes in the mask region while the photoresist remains intact in other regions (Figure 4.13 (c)). The sample was then metallized using electron beam evaporation. A 50 nm Chromium thin film was deposited. Metal liftoff using 1165 remover leaves Chromium metal mask for subsequent processing.

The next step is to create a stage layer, an etched area to accommodate the microwires separated from the bulk silicon. We suspected this step was needed to reduce the influence of the electric field of the bulk silicon. The method increases the effective aspect ratio of

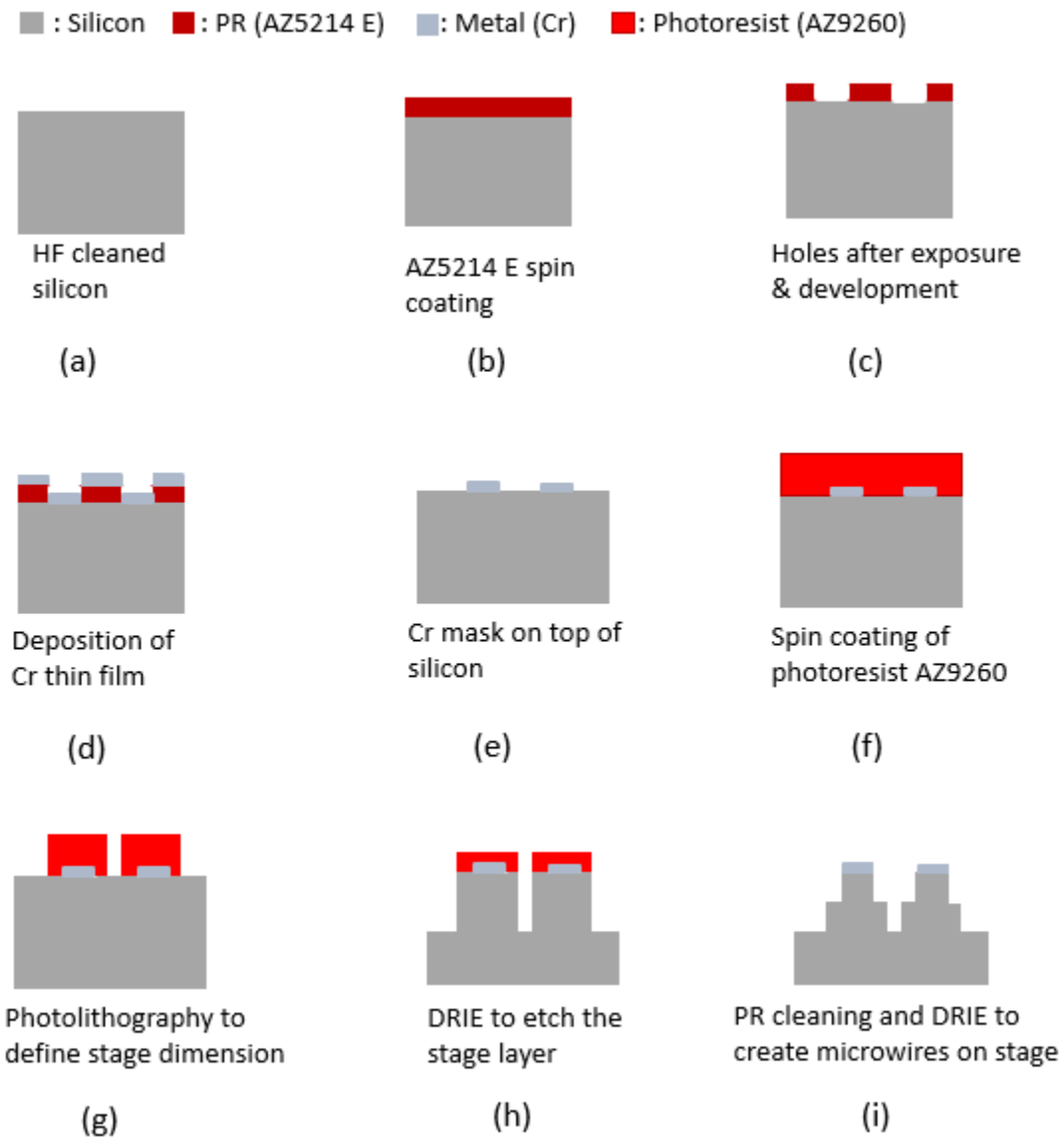

Figure 4.13: Microwire fabrication process flow with a stage layer.

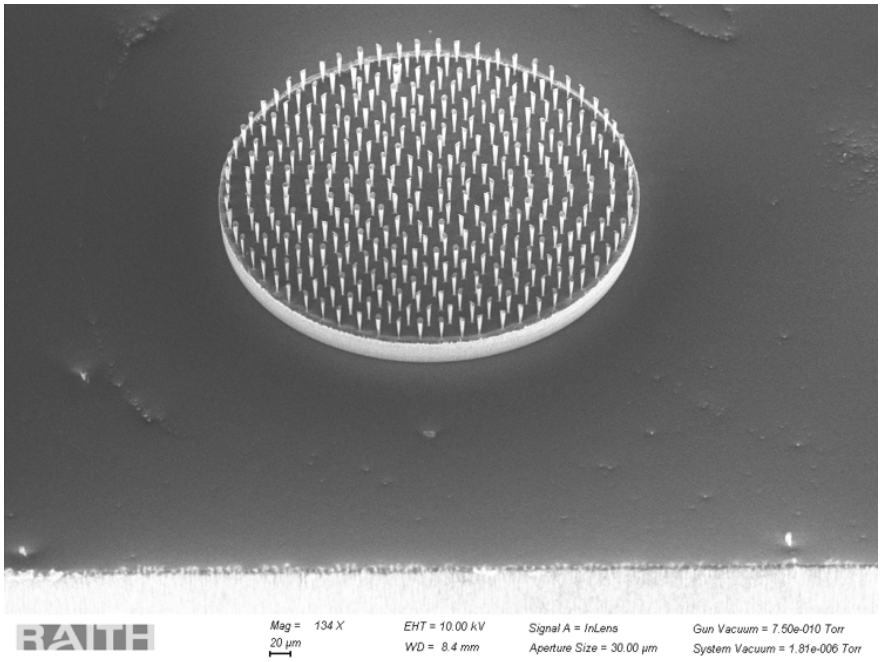

(a)

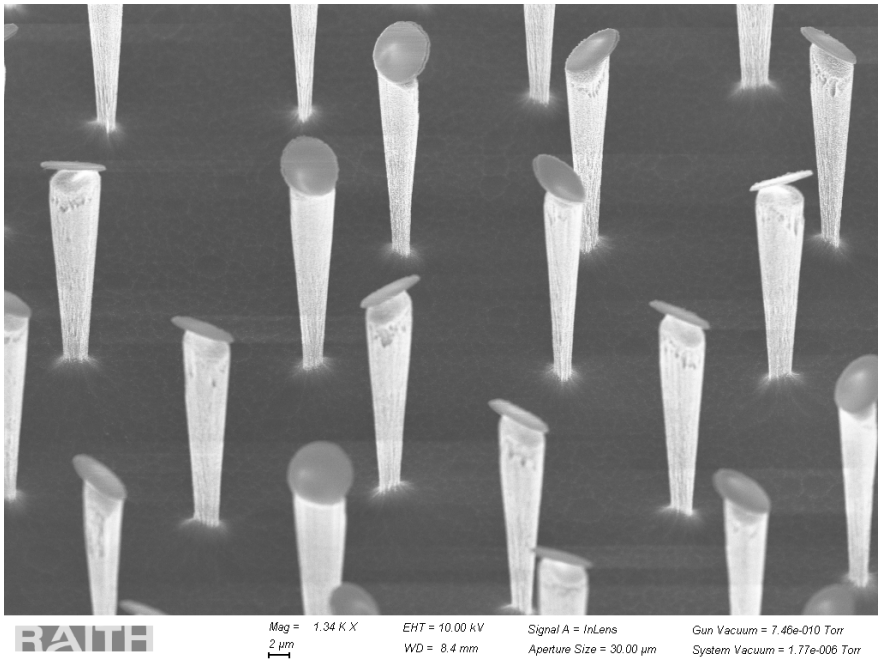

(b)

Figure 4.14: SEM images of (a) microwires with a stage layer, and (b) a zoomed image of microwires on top of the stage layer.

the microwires for which another photolithography process is needed. Photoresist AZ9260 was used to spin-coat a thick resist layer (Figure 4.13 (f)). Subsequent exposition and development results in a resist layer covering the microwire mask as shown in Figure 4.13 (g). We used DRIE to etch the stage layer at this point (Figure 4.13 (h)).

After the creation of the stage layer, the wafer was diced into 1 mm × 1 mm small dies. The cut dies were then further processed using another DRIE step to create the microwires on top of the stage layer (Figure 4.13 (i)).

Figure 4.14 shows the microwires after the second DRIE. The fabricated device has ~ 40 μm of stage depth and a microwire height of ~ 20 μm, with a tip radius of ~ 2.5 μm.

4.2.2 Assembly technique

The assembly technique is similar to the PCB-level framework used for the probe needle tests. As shown in Figure 4.15, the die is connected to the emitter PCB's front side metal pad (around a via) using a conductive epoxy. The die thickness is ~ 0.65 mm, hence a desired inter-electrode gap can be achieved, by using a suitable spacer. In our case, we used an inter-electrode gap of ~ 100 μm.

Although previously we chose a ring collector, in this experimentation we avoided it. A PCB-level grid collector was used as a collector. This is because the sharp edges of the die tend to start to act as the emitter, as it is close to the annular ring of a ring collector. Due to the limitations in PCB manufacturing capabilities, very small outlet holes can not be

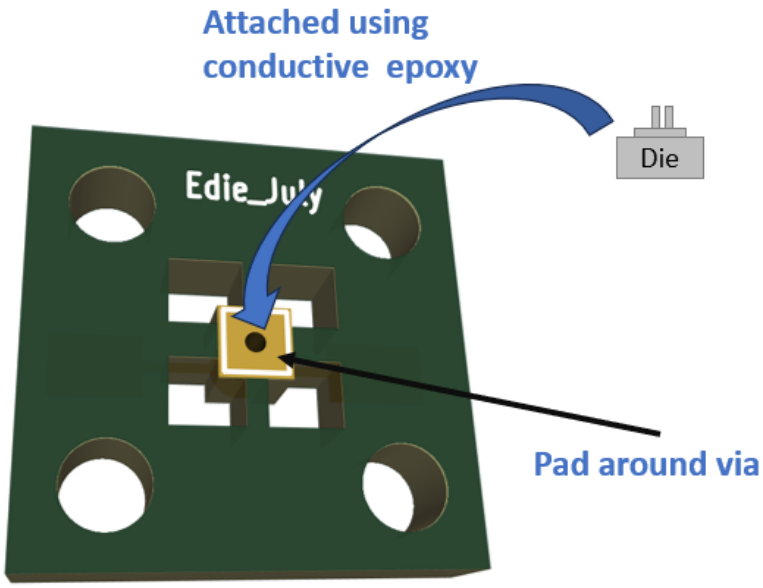

Figure 4.15: Microwire die assembly.

manufactured. In our case, we manufactured a grid with (0.4 mm × 0.4 mm) outlet holes, shown in Figure 4.16.

4.2.3 V-I characteristics

Figure 4.17 shows the VI characteristics and the fitted '$\boldsymbol{C}$' for the emitter architecture. The achieved '$\boldsymbol{C}$' of $\sim 1.91842 \times 10^{-11}\ A/V^2$ is far higher than the '$\boldsymbol{C}$' values achieved in Design 1, due to further miniaturization. A hissing sound, often related to the ionization, was recorded. The typical V-I graph confirms sustained corona generation. Important to note that the current showed more fluctuations compared to Design 1.

Although a sustained corona generation was achieved, it didn't result in a detectable

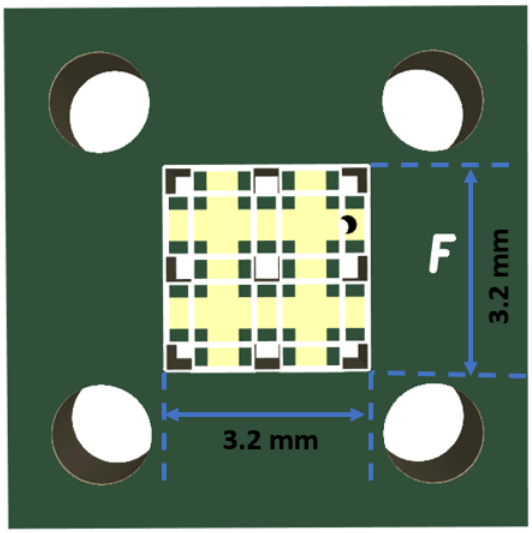

Figure 4.16: The grid used as a collector.

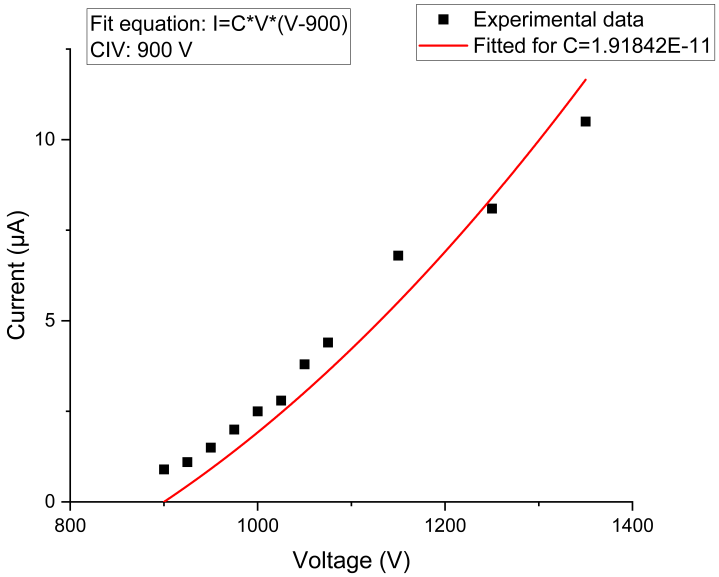

Figure 4.17: Best fitted '$\boldsymbol{C}$' in Townsend's equation (equation(3.4)) for the microwire architecture. The unit of '$\boldsymbol{C}$' is in A/V^2.

airflow. This could be for various reasons. One possible reason is the absence of a strong electric field gradient to push the ions. Normally, Peek's equation (equation (3.1)) dictates the electric field. In our setup, the bulk silicon might impact the electric field distribution. A potential way to avoid this is by increasing the stage depth and the microwire height. Moreover, the collector design is limited by the manufacturing capabilities in our framework. Both these issues can be solved using fully microfabricated devices, which we will discuss in Section 6.1.

Before moving to fully microfabricated architecture, it is important to note that the academic photolithography infrastructure that we have access to, can reach critical dimensions in the micron range. However, going to the nanoscale is a challenge with traditional lithography. It is apparent that further miniaturization of the emitter is needed to further reduce the CIV. Thus, fabricating smaller diameter nanostructures such as silicon nanowires needs other techniques to follow. The next chapter (Chapter 5) is dedicated to the demonstration of a highly controllable silicon nanowire fabrication process.

Chapter 5

Controlled Fabrication of Silicon Nanowires (SiNWs)

Part of this chapter will be submitted for publication in [94].

5.1 Silicon nanowire: an introduction

With the advent of advanced modern nanofabrication techniques, researchers have explored heavily new nanostructures and their applications. During the last few decades, a major focus was geared towards silicon nanowires (SiNWs). Silicon nanowires exhibit extraordinary electrical, mechanical, optical, and thermal properties, making them a major focus to investigate for different applications. As the world is desperately trying to find the beyond-Moore innovation that can replace the saturating CMOS technology,

nanostructures like silicon nanowires ignite special interests. There has been an enormous amount of research in silicon nanowire-based transistors and microarchitectures [95–98]. Another important area of application for SiNWs is in photovoltaics. SiNW based solar cells yield high efficiencies due to their large surface area-to-volume ratios and low reflections [99, 100]. Silicon nanowires have also been extensively used to build novel sensors with high sensitivity and small form factors. Sensory applications such as gas sensing or less-invasive blood glucose detection are some, to name a few [101, 102]. Extremely small diameter nanowires also exhibit quantum confinement, a phenomenon that results in widening the energy bandgap, which evokes much interest as well [103]. The new generation of batteries are also exploiting SiNWs-based anodes which result in extremely promising performances. The technology is already pushing the Electric Vehicle (EV) revolution through the commercialization of SiNW batteries that can provide unprecedented energy densities of 500 Wh/kg [104]. Needless to say, there has been a continuous effort to use nanowires in new non-traditional applications as well.

5.2 Common fabrication approaches

Controlling the dimensions of silicon nanowires is extremely desirable in nanotechnology, but achieving this is not straightforward. Also, different applications can beg for higher control on the alignment as well [105]. There are primarily two approaches to fabricating silicon nanowires- namely bottom-up and top-down approaches.

The most common bottom-up fabrication approach is to use VLS (vapor-liquid-solid) growth to synthesize nanowires. The method requires a metal catalyst (Au, Al, etc.) deposition, often using sputtering, which determines the diameter, density, and alignment of the nanowires [106, 107]. The reliance on sputtering thus often results in loosely controlled fabrication in terms of the nanowire dimensions. The alignment of the fabricated SiNWs is also challenging to control. The SiNWs often bend and entangle with each other, where controlling the pitch is challenging.

Metal assisted chemical etching (MACE or MACEtch) is a popular top-down method to fabricate silicon nanowires due to its inexpensive, less complex nature. In the first step, the substrate needs to be covered with metal catalyst nanoparticles, either by depositing a thin film using evaporation/sputtering or electroless deposition of the same. The substrate is then etched in an HF & H_2O_2 based solution to achieve vertical nanowires [108–110]. The process needs the metal film to be porous, as the area under the metal catalyst is etched away, and the un-patterned/holey area withstands the etching process, resulting in free-standing SiNWs. Again, the random nature of nanoparticle deposition causes uncontrolled nanowire growth. The process is also crystal orientation dependent, as the orientation dictates the growth direction of the nanowires. One way to increase the controllability is to use nanospheres to define the diameter [111]. This process increases the control of the nanowire diameter, but achieving the required density and spacing still remains a challenge, primarily due to the inability to control the deposition of nanospheres and metal thin film porosity. In [112],

the authors used a slightly modified approach, where they used electron beam lithography (EBL) to define the metal mask, then subsequently to MACEtch (etch) the exposed area to produce nanowires. The authors mentioned the existence of nanogaps around the nanowires, which can change the etching process. Moreover, the thickness and porosity of the thin film remain a key factor for the successful implementation of the process. There have been many works on fabricating horizontal silicon nanowires using electron beam lithography [113,114], but vertically aligned silicon nanowire fabrication is mostly dominated by MACE, which has several concerns, as discussed earlier.

In this work, we propose a method that combines EBL and deep reactive ion etching (DRIE) to fabricate highly controlled silicon nanowires. The direct writing process eliminates the requirement of a physical mask (which often incurs additional cost and delay to the process), whereas the DRIE process provides a vertical anisotropic etching profile for the nanowires. EBL also makes the process shape-independent, unlike MACE. The flexibility in digital mask design results in an easily tuneable nanowire shape.

First, the fabrication process flow is explained here, and then the measurements and analysis are discussed, followed by the conclusions.

5.3 Process flow

We used a p-type $< 100 >$ silicon substrate with a resistivity of 0.003-0.005 Ω.cm. EBL was used to create the mask to have controlled fabrication of SiNWs, and DRIE was used to etch

the bulk silicon. The complete fabrication process flow is shown in Figure 5.1.

5.3.1 Spin coating

At first, the sample was dipped into HF to remove the native oxide and rinsed with DI water, as shown in Figure 5.1 (a). The sample was then dried and pre-baked at 180°C for 5 minutes on a hotplate. We opted for positive EBL resist polymethyl methacrylate (PMMA) 950K A4 to coat the sample, as shown in Figure 5.1 (b). Spin coating was employed to achieve a resist thickness of $\sim$ 200 nm. The sample was then hotplate-baked again at 180°C for 90 seconds.

5.3.2 Electron beam lithography (EBL) & development

The purpose of this research is to investigate the controllability of silicon nanowire growth for different diameter nanowires. The EBL writing was thus designed into 3 groups to characterize the nanowire density and diameter, as follows,

1. **Group 1**: Matrix of 200 nm diameter circles, with 200 nm inter-nanowire spacing.
2. **Group 2**: Matrix of 400 nm diameter circles, with 400 nm inter-nanowire spacing.
3. **Group 3**: Matrix of 600 nm diameter circles, with 600 nm inter-nanowire spacing.

The EBL parameters have been listed in Table 5.1. Among the parameters listed, dose is found to be the most important factor. The choice of energy dose can significantly impact

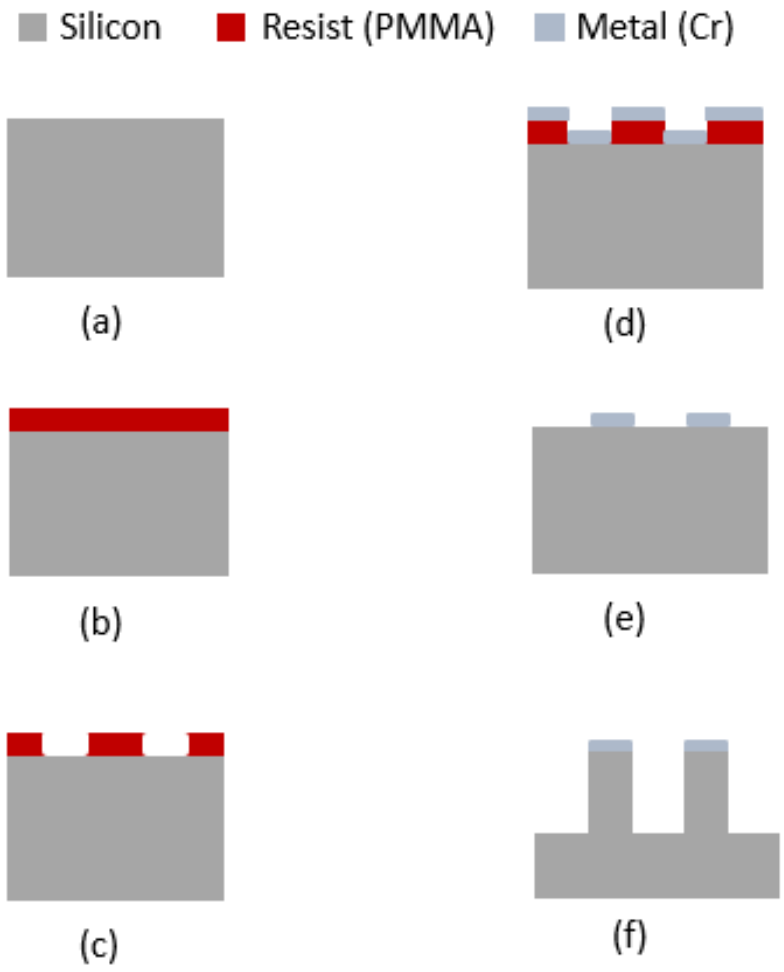

Figure 5.1: Fabrication process flow: (a) HF cleaned silicon substrate. (b) Sample after spin coating with PMMA. (c) Sample after EBL and development. (d) Thin film deposited sample, using Electron beam evaporation. (e) Metal (Cr) mask after lift-off. (f) Free-standing vertical nanowires, after the etching process.

the exposure process and the resolution of the nanostructures. Also, the dose needs to be calibrated for each geometry.

Parameter	Value
Nanostructures	Circles
Acceleration voltage	10 kV
Dose	100 $\mu C/cm^2$
Aperture	30 μm
Working distance	10 mm

Table 5.1: Electron beam lithography (EBL) parameters.

After exposure, the development was done using a solution of MIBK: IPA (1:3) for 60 seconds. The sample was subsequently rinsed with IPA (Isopropyl alcohol) for 15 seconds and finally dried using nitrogen. The development process creates circular holes in the PMMA film, as shown in Figure 5.1 (c).

5.3.3 Metallization & liftoff

A 50 nm layer of chromium was then deposited using e-beam evaporation (Figure 5.1 (d)) and patterned using lift-off in acetone (Figure 5.1 (e)) with agitation. The metal thickness was selected to be enough as a hard mask for subsequent DRIE-etching of the nanowires up to the desired length. The PMMA thickness was set to be more than 3 times the metal thickness to facilitate the lift-off process.

Parameter	Value
Metal	Chromium (Cr)
Base Vacuum	2.4×10^{-6} Torr
Deposition rate	1 Å/s
Film thickness	50 nm
Emission current	38 mA

Table 5.2: Electron beam evaporation parameters

5.3.4 Deep reactive ion etching (DRIE)

After the Chromium mask was created, the exposed silicon sample was then etched using the DRIE Bosch process. In [115], the authors have shown that nanowires with scalloping can be a better choice for higher optical absorption, instead of nanowires with smooth sidewall profiles. This method can be a good choice, as the scalloping can be tuned based on the DRIE passivation/etching time. There have been previous efforts to fabricate silicon nanowires using traditional reactive ion etching (RIE), but they lacked in serval aspects [116,117]. The structure generated by the RIE etching often lacks the vertical anisotropicity required. Most importantly, reaching higher depth may be a challenge with RIE.

5.4 Characterization & Results

Some part of Group 2 was intentionally scratched to get a good view of the sidewalls of the nanowires. Figure 5.2 indicates the height of the nanowires in this region to be $\sim$ 2.5 µm (aspect ratio of 6).

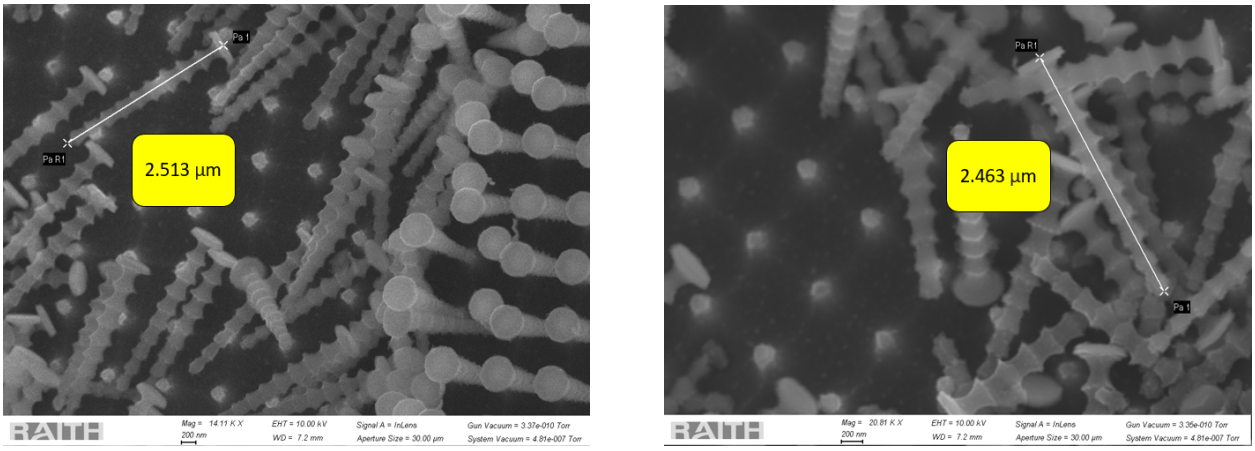

Figure 5.2: Height of the nanowires (Group 2).

We also looked into the fabricated nanowires and whether they meet our expected dimensions, based on our EBL writing. We investigated the fabricated diameter, pitch, and the alignment.

Figure 5.3 (a) shows the tilted top view of the fabricated silicon nanowire array in Group 1. This group has the least diameter and least spacing between the nanowires, causing a denser jungle of nanowires. Figure 5.3 (b) shows the nanowire diameter and the inset shows the pitch. The SiNWs have some Chromium left on their tips.

The SEM images of Group 2 are shown in Figure 5.4. The tilted top view of Figure 5.4 (a) indicates highly aligned vertical nanowire growth. The nanowires look evenly separated and well-aligned. The metal mask clearly remains intact, which again can be removed using a Cr etchant if needed.

Similar to Group 2, Group 3 also exhibits extreme control and vertical alignment of the nanowires, as shown in Figure 5.5. Such anisotropic etching would be difficult with RIE.

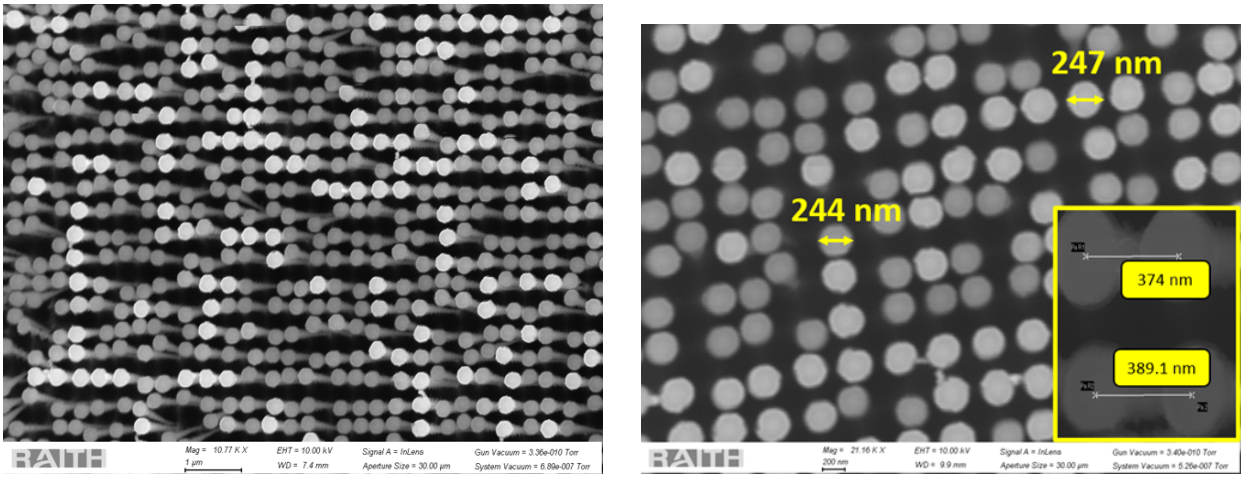

(a) **(b)**

Figure 5.3: SEM images of the silicon nanowires in Group 1, with (a) a 3D view and (b) diameter & pitch (in inset) from the top view.

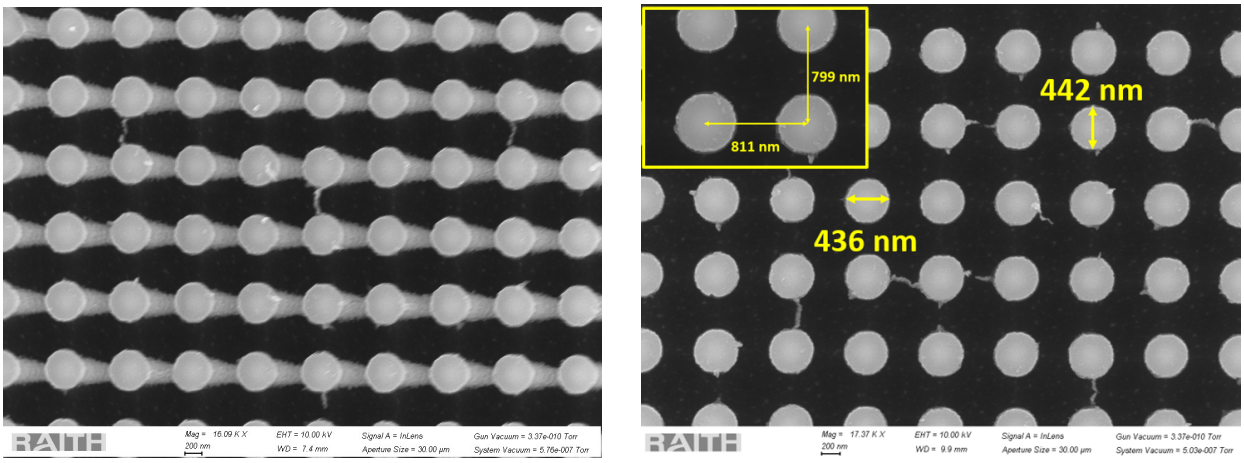

(a) **(b)**

Figure 5.4: SEM images of the silicon nanowires in Group 2, with (a) a 3D view and (b) diameter & pitch (in inset) from the top view.

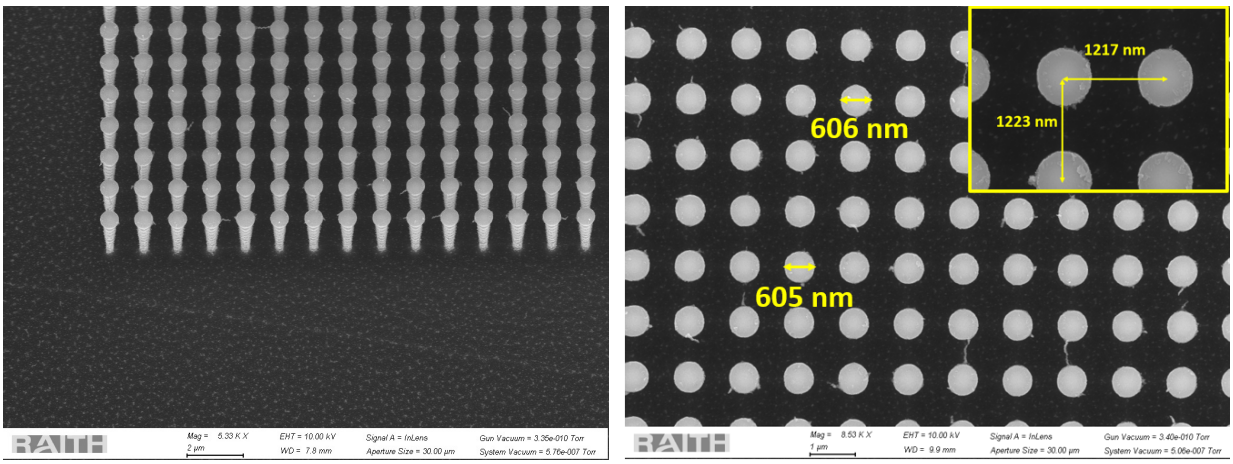

(a) **(b)**

Figure 5.5: SEM images of the silicon nanowires in Group 3, with (a) an overall view and (b) diameter & pitch (in inset) from the top view.

All SEM photos of the three different groups, as shown in Figures 5.3, 5.4, and 5.5, with measurements of the nanowire diameters and pitch also confirm the proper vertical alignment of the nanowires. The scalloping effect resulting from the Bosch process is also evident in Figure 5.4 (a) & Figure 5.5 (a).

5.5 Analysis

In this section, we have analyzed the nanowire dimensions (diameter and spacing/pitch) using ImageJ software. Table 5.3 shows that we can rely on the presented process to fabricate nanowires controllably. All three groups show extreme predictability of nanowire pitch, with a fabrication error of less than 2%. This extraordinary precision can be leveraged in areas

where pitch is of utmost importance. In terms of the nanowire diameter, Group 3 shows the best predictability, with less than 4% deviation from the mask patterns. In Group 1, the nanowires with the least pitch (400 nm pitch at mask level) and least diameter (200 nm) show the highest error in average diameter, which is close to 25%. The deviation can be improved by improving the EBL resolution (by optimizing area doses, focus, etc.) and lift-off.

Parameters	Group 1	Group 2	Group 3
Diameter (mask)	200 nm	400 nm	600 nm
Average diameter (fabricated)	251.6 nm	445 nm	623.9 nm
Average diameter (error)	25%	11.25%	4%
Average pitch (mask)	400 nm	800 nm	1200 nm
Average pitch (fabricated)	403.1 nm	816 nm	1221.7 nm
Average pitch (error)	0.77%	2%	1.8%

Table 5.3: Fabricated device analysis.

In this work, a highly controllable method of fabricating silicon nanowires was presented. The method is based on EBL and DRIE to provide superior control over nanowire diameter/pitch and length. The know-how of SiNW fabrication is essential for complete microfabrication, discussed in the next chapter.

Chapter 6

Future Works

In this chapter, a novel fully microfabricated ion thruster design technique is proposed. The fully microfabricated devices will employ microwires/nanowires as emitters, fabricated using the techniques previously mentioned. This section also comments on a few major roadblocks regarding applications and commercialization.

6.1 Complete microfabrication

It is evident from earlier discussions that a completely silicon microfabricated EHD device would be extremely desirable. Parameters such as the desired positioning/alignment of the emitter, the inter-electrode gap, etc., are extremely hard to control and potentially add errors to the results due to the manual assembly. Fully microfabricated devices will ensure keeping such errors within a few microns, yielding much more accurate and repeatable results. The

following section explains the process flow of a novel chip-level micro ion thruster design technique, which is unique in its ability to customize all geometrical parameters that impact the device's performance.

6.1.1 Process flow

The complete fabrication of micro ion thrusters requires processing 2 wafers. Wafer 1 is used to create the emitters and the inlet holes. Wafer 2 is used to create the collector, with defined outlet holes. Both wafers are bonded together, where the bonding material's thickness controls the inter-electrode gap. Moreover, it will overcome the challenges faced in the previous chapter.

A low resistivity double-side polished (DSP) silicon wafer could be used for Wafer 1 processing. The first step is to deposit silicon dioxide (SiO_2) using thermal evaporation, followed by spin coating of a photoresist, as shown in Figure 6.1 (a, b). Photolithography and subsequent SiO_2 etching & PR removal will create a rectangular exposed silicon area with a boundary of SiO_2, as shown in Figure 6.1 (c, d). The exposed silicon will define the channel, the size of which can be controlled using the lithography mask. The wafer will need to be coated with EBL resist (PMMA), and subsequent direct writing, development, metallization (Cr using EBE), and metal lift-off processes will create a metal mask for nanowire/microwire fabrication (steps e-h). The EBL hole dimensions determine the nanowire diameter. The SiNW fabrication technique was explained in Chapter 5. The next

few steps involve processing the other polished side of Wafer 1 to define the emitter side inlet holes. Figure 6.1 (i-l) shows the traditional lithography and metallization process to create a metal mask on the back side of the wafer. Later, DRIE can be used to create through-holes (step m), where the metal layer protects the outer boundary and pillars. Shown in Figure 6.1 (m) are the inlet holes that need to be optimized. The dimensions can be tuned by controlling the metal mask design. Lastly, aluminum is deposited using sputtering to create metal pads. Although the sputtering process will add some metal to the sidewalls, it shouldn't have any negative impact.

A low resistivity (device layer) DSP SOI (Silicon on Insulator) wafer is to be taken for Wafer 2 processing. First, an SU-8 layer is spin-coated on the device layer of Wafer 2, and photolithography is employed to create a boundary similar to Wafer 1. Next is to bond 2 wafers (Wafer 1 & Wafer 2) together, as shown in Figure 6.2 (c). The SU-8 layer is used not just for bonding, but also to separate the emitter and collector sides electrically. SU-8 adhesive bonding has proved to be a good choice for this purpose, with many successful demonstrations in several earlier works [118–120]. After bonding, the substrate or handle layer silicon of the SOI wafer is etched away with DRIE and the oxide layer is removed using HF vapor, as shown in Figures 6.2 (d, e). Photolithography, metallization, and liftoff have been used on the remaining device layer to create a metal mask, in order to define the outlet holes (steps f-i). The final DRIE not only creates the outlet holes but also etches the emitter side pillars with a metal mask, resulting in nanowires/microwires Figure 6.2 (j).

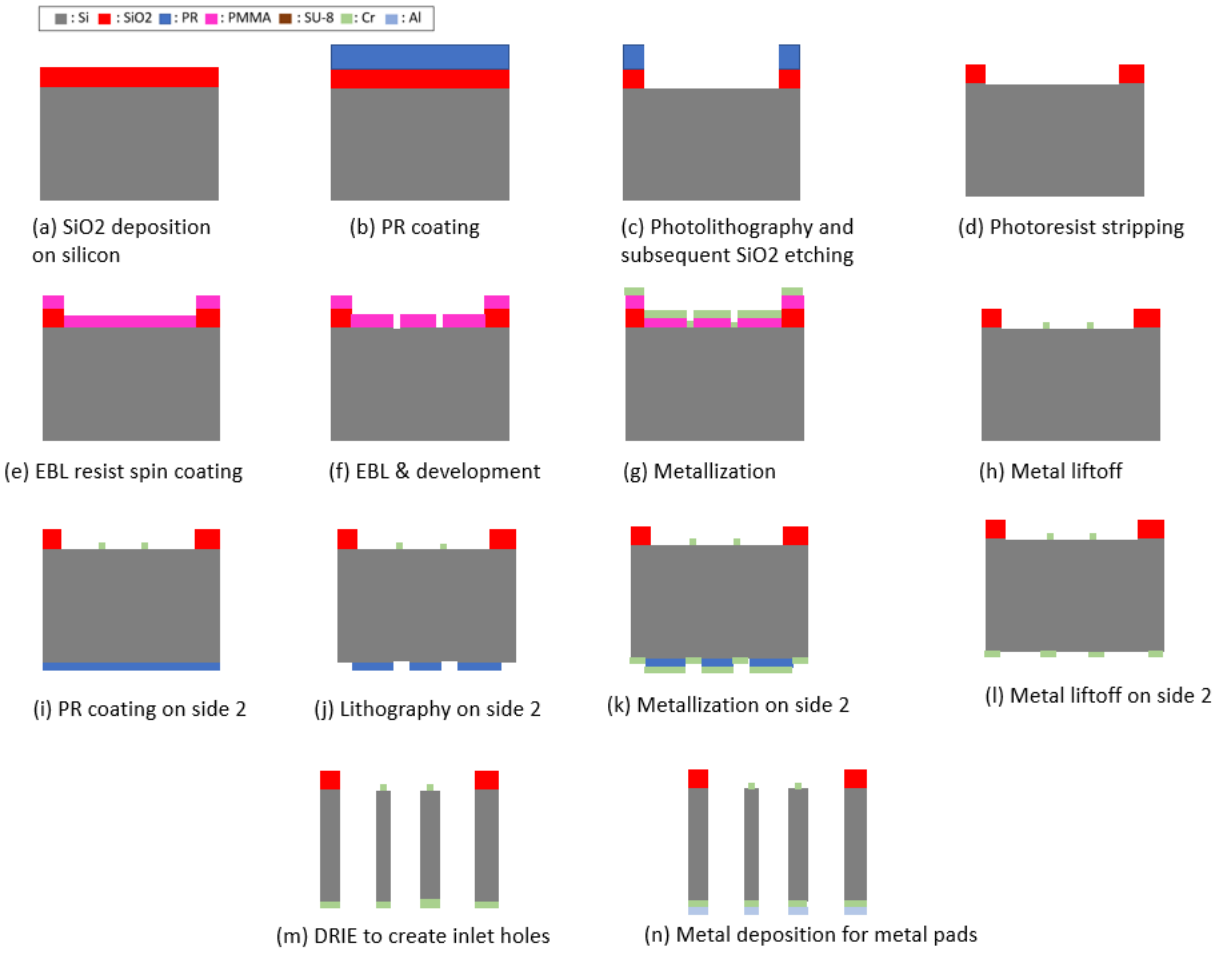

Figure 6.1: Wafer 1 (Silicon) processing: Microfabrication steps required to fabricate the emitter wafer, with defined inlet dimensions.

The overall process requires extreme care to protect the nanowires/microwires due to their fragility. The nanowires/microwires are created at the very end in order to safeguard them. The SU-8 layer and oxide layer together dictate the inter-electrode gap, which obviously is controllable with nanoscale resolution. The SU-8 film thickness can be varied from a few microns to hundreds of microns. This gives greater flexibility to fabricate devices with a wide range of inter-electrodes gaps.

The process results in a multi-emitter needle-to-grid architecture. Needless to say, the base process can easily be modified to produce different geometrical features and architectures.

6.1.2 Expected improvements

Apart from the great controllability, completely microfabricated devices improve the overall performance of the system as well. If the channel & collector dimensions, emitter radius, and inter-electrode gap remain the same, similar output airflow or thrust can be expected. Thus, the device will have very little weight compared to the PCB-level framework we used, resulting in an extremely high thrust-to-weight ratio. With a small outlet area, we also expect a very high thrust density. With a confined gap to reduce losses and lower operating voltages, the device could exhibit high efficiency as well. Moreover, such devices will be thinner to accommodate for electronic cooling. 3D IC packaging is considered one of the most popular technologies to extend Moore's law. One of the biggest challenges for

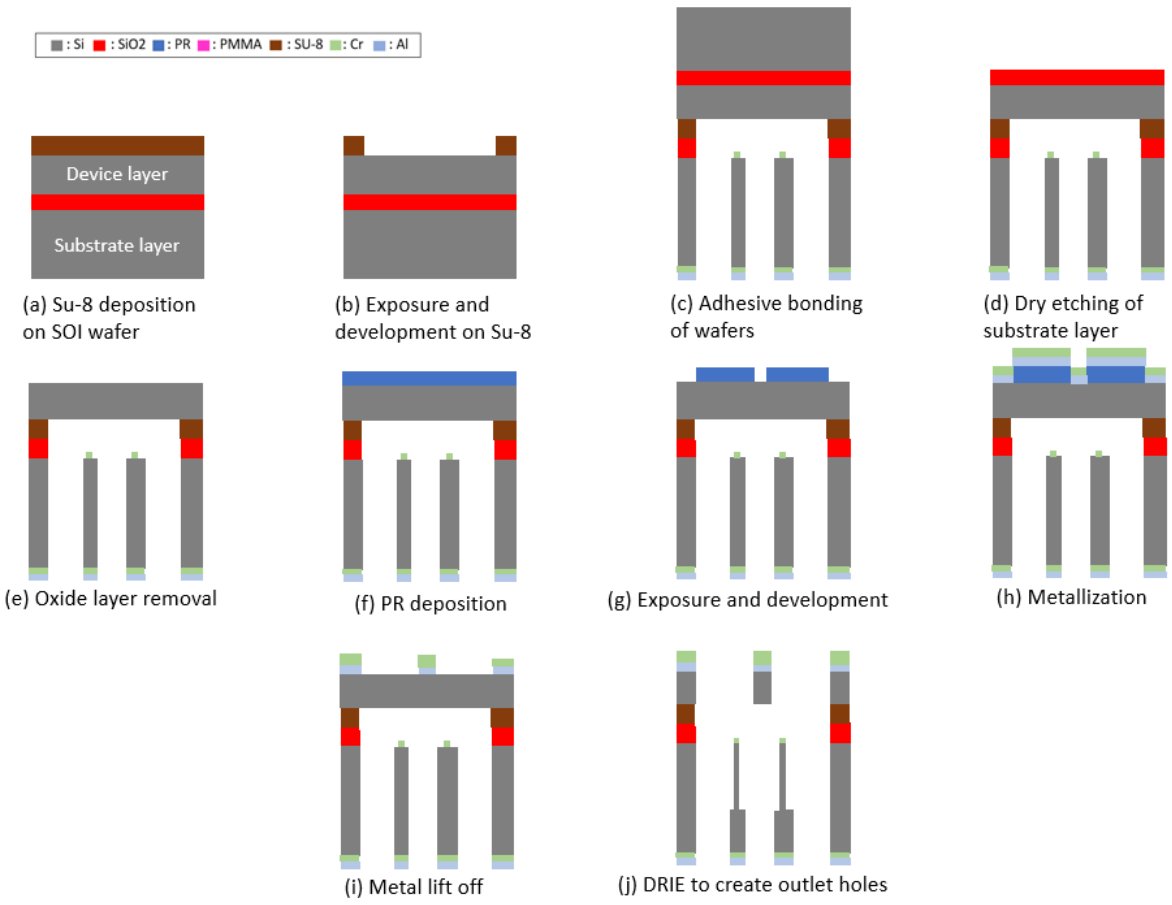

Figure 6.2: Bonding and Wafer 2 (SOI) processing: After bonding 2 wafers, the processing on the SOI wafer creates the collector and outlet holes.

this advanced packaging technique is thermal management [121–125]. The proposed "all-silicon" ion thruster is compatible with modern semiconductor fabrication techniques and can potentially be used in some stacks of 3D ICs, opening a new horizon for integrated chip-level cooling solutions. Fully microfabricated ion thrusters are almost non-existent in the literature, with Drew's works being the outlier [13]. Even Drew's work required some amount of manual assembly of microfabricated parts, which added error and is a hindrance to scalability. The methodology introduced here completely resolves these problems by removing any manual assembly requirements.

6.2 Major roadblocks

The technology is at a very nascent stage and is still to overcome some major obstacles before it becomes suitable for commercialization.

6.2.1 The reliability woe

One of the greatest concerns related to the technology is the reliability of the overall system. It is very common to have fractures/tears in the coronating electrode after a few hours of operation [126, 127]. The discharge current drops after long operation, reducing the performance of the device. Extensive research is needed to eliminate or drastically limit the impact of this on performance.

One way to improve the reliability is by coating the emitter with a protective layer.

Drew, in his work, used TiN coating to reduce the performance degradation [126]. Ong [127] chose to use palladium coating and showed that the coating thickness is of importance as well. The coating will have an impact on the operational voltage, as it will increase the emitter diameter, increasing the CIV- another trade-off to be kept in mind. Commercial electronic devices require a high MTTF (mean time to failure) to be commercially viable and acceptable. This is still a far-fetched goal. Moving forward, research in material science and the search for the ideal electrodes is essential to tackle the reliability challenges. For example, Carbon nanotubes (CNTs) have been experimentally verified to generate plasma at a very low voltage [128, 129]. With excellent electro-mechanical properties, whether CNTs can be used for low voltage EHD applications is yet to be answered.

6.2.2 Application-specific challenges

Envisioning a world of small EHD micro-robots or microbots is only possible if significant improvement in the miniaturization of batteries, voltage converters and control electronics is possible, in order to reduce the overall weight of the device.

The technology has enormous potential in cooling applications, especially because of its tunable size and integrability with the semiconductor fabrication processes. A chip-level integration of the technology will not just require mechanical considerations, but innovation in the packaging technology, the power distribution networks (PDN), the optimization of real estate, etc.

Chapter 7

Conclusion

This work investigated thoroughly the need for the miniaturization of ion thrusters and demonstrated two novel designs. One key objective of the research was to reduce the operational voltage. Both designs have successfully demonstrated a significant reduction in the operational voltage by means of miniaturization. The achieved airflow is good enough to use in electronic cooling, based on the literature. On the other hand, for propulsion applications, a high thrust density ($> 40\ N/m^2$) was achieved. With a thrust density of $\sim 40\ N/m^2$, a millimeter-scale system with a mass of 250 mg can be lifted with an outlet size of just $\sim 62.3\ mm^2$. Thus, complete microfabrication holds the key to future growth in this domain.

The commercialization of EHD-based systems requires much more interdisciplinary research, not just in the fundamental technology but also in peripheral technologies for

specific applications. Although propulsion and cooling remain the two main applications, the technology can potentially transcend to unexplored applications, where large form factor and voltage requirements have been the greatest barriers. Efforts to fully microfabricate devices have been astonishingly small, and there is a huge room for improvement.

Finally, the work should serve as a stepping-stone for future researchers toward the realization of low voltage efficient microscale EHD system designs.

Bibliography

[1] S. Mukherjee, M. Y. Elsayed, H. H. Tawfik, and M. N. El-Gamal, "Demystifying the impact of electrode gap and emitter radius in designing miniaturized ion thrusters based on DC corona discharge." Manuscript to be submitted for publication, 2024.

[2] A. Yehia, M. Abdel-Salam, and A. Mizuno, "On assessment of ozone generation in dc coronas," *Journal of Physics D: Applied Physics*, vol. 33, no. 7, p. 831–835, 2000.

[3] X. Li, X. Cui, T. Lu, D. Li, B. Chen, and Y. Fu, "Influence of air pressure on the detailed characteristics of corona current pulse due to positive corona discharge," *Physics of Plasmas*, vol. 23, no. 12, 2016.

[4] Z. Yuan, K. Suzuki, Y. Ehara, J. Ikeda, K. Yamashiro, and T. Takano, "Corona discharge characteristics in electrostatic precipitator under high temperature," in *2020 IEEE Industry Applications Society Annual Meeting*, pp. 1–6, 2020.

[5] A. Yawootti, P. Intra, N. Tippayawong, and P. Rattanadecho, "An experimental study of relative humidity and air flow effects on positive and negative corona discharges in

a corona-needle charger," *Journal of Electrostatics*, vol. 77, p. 116–122, 2015.

[6] S. Chen, K. Li, F. Wang, Q. Sun, and L. Zhong, "Effect of humidity and air pressure on the discharge modes transition characteristics of negative dc corona," *IET Science, Measurement amp;amp; Technology*, vol. 13, p. 1212–1218, Oct 2019.

[7] K. Holste, P. Dietz, S. Scharmann, K. Keil, T. Henning, D. Zschätzsch, M. Reitemeyer, B. Nauschütt, F. Kiefer, F. Kunze, and et al., "Ion thrusters for electric propulsion: Scientific issues developing a niche technology into a game changer," *Review of Scientific Instruments*, vol. 91, no. 6, p. 061101, 2020.

[8] I. Levchenko, K. Bazaka, Y. Ding, Y. Raitses, S. Mazouffre, T. Henning, P. J. Klar, S. Shinohara, J. Schein, L. Garrigues, and et al., "Space micropropulsion systems for cubesats and small satellites: From proximate targets to furthermost frontiers," *Applied Physics Reviews*, vol. 5, no. 1, 2018.

[9] P. A. Walsh, V. Egan, R. Grimes, and E. Walsh, "Scaling of flow characteristics and power consumption with profile height for miniature centrifugal fans," *ASME 5th International Conference on Nanochannels, Microchannels, and Minichannels*, 2007.

[10] N. E. Jewell-Larsen, G. G. Joseph, and K. A. Honer, "Scaling laws for electrohydrodynamic air movers," *ASME/JSME 2011 8th Thermal Engineering Joint Conference*, 2011.

[11] Z. Zhang, X. Wang, and Y. Yan, "A review of the state-of-the-art in electronic cooling," *e-Prime - Advances in Electrical Engineering, Electronics and Energy*, vol. 1, p. 100009, 2021.

[12] H. H. Radamson, H. Zhu, Z. Wu, X. He, H. Lin, J. Liu, J. Xiang, Z. Kong, W. Xiong, J. Li, and et al., "State of the art and future perspectives in advanced cmos technology," *Nanomaterials*, vol. 10, no. 8, p. 1555, 2020.

[13] D. S. Drew, N. O. Lambert, C. B. Schindler, and K. S. J. Pister, "Toward controlled flight of the ionocraft: A flying microrobot using electrohydrodynamic thrust with onboard sensing and no moving parts," *IEEE Robotics and Automation Letters*, vol. 3, no. 4, pp. 2807–2813, 2018.

[14] H. K. Hari Prasad, R. S. Vaddi, Y. M. Chukewad, E. Dedic, I. Novosselov, and S. B. Fuller, "A laser-microfabricated electrohydrodynamic thruster for centimeter-scale aerial robots," *PLOS ONE*, vol. 15, no. 4, 2020.

[15] N. T. Jafferis, E. F. Helbling, M. Karpelson, and R. J. Wood, "Untethered flight of an insect-sized flapping-wing microscale aerial vehicle," *Nature*, vol. 570, no. 7762, p. 491–495, 2019.

[16] Y. M. Chukewad, A. T. Singh, J. M. James, and S. B. Fuller, "A new robot fly design that is easier to fabricate and capable of flight and ground locomotion," in

2018 IEEE/RSJ International Conference on Intelligent Robots and Systems (IROS), pp. 4875–4882, 2018.

[17] Y. M. Chukewad, J. James, A. Singh, and S. Fuller, "Robofly: An insect-sized robot with simplified fabrication that is capable of flight, ground, and water surface locomotion," *IEEE Transactions on Robotics*, vol. 37, no. 6, pp. 2025–2040, 2021.

[18] T. A. Ward, C. J. Fearday, E. Salami, and N. Binti Soin, "A bibliometric review of progress in micro air vehicle research," *International Journal of Micro Air Vehicles*, vol. 9, no. 2, p. 146–165, 2017.

[19] K. Y. Ma, P. Chirarattananon, S. B. Fuller, and R. J. Wood, "Controlled flight of a biologically inspired, insect-scale robot," *Science*, vol. 340, no. 6132, p. 603–607, 2013.

[20] R. Wood, "Fly, robot, fly," *IEEE Spectrum*, vol. 45, no. 3, pp. 25–29, 2008.

[21] Y. Chen, H. Zhao, J. Mao, P. Chirarattananon, E. F. Helbling, N.-s. P. Hyun, D. R. Clarke, and R. J. Wood, "Controlled flight of a microrobot powered by soft artificial muscles," *Nature*, vol. 575, no. 7782, p. 324–329, 2019.

[22] Y. Kubo, I. Shimoyama, and H. Miura, "Study of insect-based flying microrobots," in *[1993] Proceedings IEEE International Conference on Robotics and Automation*, pp. 386–391 vol.2, 1993.

[23] T. Yamamoto, W. Maeda, Y. Ehara, and H. Kawakami, "Development of ehd-enhanced plasma electrostatic precipitator," in *2011 IEEE Industry Applications Society Annual Meeting*, pp. 1–7, 2011.

[24] A. Afshari, L. Ekberg, L. Forejt, J. Mo, S. Rahimi, J. Siegel, W. Chen, P. Wargocki, S. Zurami, and J. Zhang, "Electrostatic precipitators as an indoor air cleaner—a literature review," *Sustainability*, vol. 12, p. 8774, Oct 2020.

[25] Y. Chun, A. Berezin, D. Brocilo, J. Mizeraczyk, and J.-S. Chang, "Modelling of near corona wire electrohydrodynamic flow in a wire-plate electrostatic precipitator," in *CEIDP '05. 2005 Annual Report Conference on Electrical Insulation and Dielectric Phenomena, 2005.*, pp. 478–481, 2005.

[26] Y. Lee, Y.-S. Kim, B. Han, Y.-J. Kim, and H.-J. Kim, "Extremely low ozone emission electrostatic compact air purifier using carbon fiber ionizers and carbon film collection stage," in *2020 IEEE Industry Applications Society Annual Meeting*, pp. 1–7, 2020.

[27] O. v. Guericke, *Experimenta Nova (ut vocantur) Magdeburgica de vacuo spatio.* J. Jansson à Waesberge, Amsterdam, 1672.

[28] F. Hauksbee, *Physico-mechanical experiments on various subjects.* London, 1709.

[29] M. Robinson, "A history of the electric wind," *American Journal of Physics*, vol. 30, no. 5, p. 366–372, 1962.

[30] M. Robinson, "Movement of air in the electric wind of the corona discharge," *Transactions of the American Institute of Electrical Engineers, Part I: Communication and Electronics*, vol. 80, no. 2, pp. 143–150, 1961.

[31] A. Martins and M. Pinheiro, "On the propulsive force developed by asymmetric capacitors in a vacuum," *Physics Procedia*, vol. 20, p. 112–119, 2011.

[32] F. X. Canning, C. Melcher, and E. Winet, "Asymmetrical capacitors for propulsion," tech. rep., Fairmont, West Virginia, 2004.

[33] T. T. Brown, "Electrokinetic apparatus," Aug 1960.

[34] J. Sovey, V. Rawlin, and M. Patterson, "A synopsis of ion propulsion development projects in the united states - sert i to deep space 1," *35th Joint Propulsion Conference and Exhibit*, 1999.

[35] G. E. Hagen, "Flying apparatus," Feb 1964.

[36] E. A. CHRISTENSON and P. S. MOLLER, "Ion-neutral propulsion in atmospheric media.," *AIAA Journal*, vol. 5, no. 10, p. 1768–1773, 1967.

[37] K. Masuyama and S. R. Barrett, "On the performance of electrohydrodynamic propulsion," *Proceedings of the Royal Society A: Mathematical, Physical and Engineering Sciences*, vol. 469, no. 2154, p. 20120623, 2013.

[38] E. Moreau, N. Benard, J.-D. Lan-Sun-Luk, and J.-P. Chabriat, "Electrohydrodynamic force produced by a wire-to-cylinder dc corona discharge in air at atmospheric pressure," *Journal of Physics D: Applied Physics*, vol. 46, no. 47, p. 475204, 2013.

[39] N. Monrolin, F. Plouraboué, and O. Praud, "Electrohydrodynamic thrust for in-atmosphere propulsion," *AIAA Journal*, vol. 55, no. 12, p. 4296–4305, 2017.

[40] K. N. Kiousis, A. X. Moronis, and W. G. Fruh, "Electro-hydrodynamic (ehd) thrust analysis in wire-cylinder electrode arrangement," *Plasma Science and Technology*, vol. 16, no. 4, p. 363–369, 2014.

[41] G. Sharma, N. P. Nambisan, O. Sarath, and T. P. Vishnu, "Design and prototype of flyback transformer driven electro hydrodynamic thruster," in *2016 7th India International Conference on Power Electronics (IICPE)*, pp. 1–4, 2016.

[42] L. Zhao and T.-M. Liaw, "Thrust origin in ehd lifters," in *2011 IEEE Industry Applications Society Annual Meeting*, pp. 1–5, 2011.

[43] M. Einat and R. Kalderon, "High efficiency lifter based on the biefeld-brown effect," *AIP Advances*, vol. 4, no. 7, 2014.

[44] P. Huang, Z.-y. Xie, P. Liu, D.-p. Leng, J.-p. Zheng, and S. Wang, "Ionic wind simulation of wire-aluminum foil electrode structure lifter in 2-d space," *IEEE Transactions on Plasma Science*, vol. 50, no. 3, pp. 566–573, 2022.

[45] L. Zhao and K. Adamiak, "Ehd gas flow in electrostatic levitation unit," *Journal of Electrostatics*, vol. 64, no. 7–9, p. 639–645, 2006.

[46] H. Xu, Y. He, K. L. Strobel, C. K. Gilmore, S. P. Kelley, C. C. Hennick, T. Sebastian, M. R. Woolston, D. J. Perreault, and S. R. Barrett, "Flight of an aeroplane with solid-state propulsion," *Nature*, vol. 563, p. 532–535, Nov 2018.

[47] F. Yang, N. E. Jewell-Larsen, D. L. Brown, K. Pendergrass, D. A. Parker, I. A. Krichtafovitch, and A. V. Mamishev, "Corona driven air propulsion for cooling of electronics," in *XIIIth International Symposium on High Voltage Engineering*, 2003.

[48] N. E. Jewell-Larsen, S. V. Karpov, I. A. Krichtafovitch, V. Jayanty, C.-P. Hsu, and A. V. Mamishev, "Modeling of corona-induced electrohydrodynamic flow with comsol multiphysics," in *Proc. ESA Annual Meeting on Electrostatics 2008*, no. Paper E1, 2008.

[49] N. E. Jewell-Larsen, H. Ran, Y. Zhang, M. K. Schwiebert, K. A. H. Tessera, and A. V. Mamishev, "Electrohydrodynamic (ehd) cooled laptop," in *2009 25th Annual IEEE Semiconductor Thermal Measurement and Management Symposium*, pp. 261–266, 2009.

[50] J. L. Lee and R. L. Blanco, "Methods and apparatus for cooling electronic devices," Nov 2012.

[51] D. Schlitz and V. Singhal, "An electro-aerodynamic solid-state fan and cooling system," in *2008 Twenty-fourth Annual IEEE Semiconductor Thermal Measurement and Management Symposium*, pp. 46–49, 2008.

[52] C.-P. Hsu, N. E. Jewell-Larsen, I. A. Krichtafovitch, S. W. Montgomery, J. T. Dibene, and A. V. Mamishev, "Miniaturization of electrostatic fluid accelerators," *Journal of Microelectromechanical Systems*, vol. 16, no. 4, pp. 809–815, 2007.

[53] C. P. Hsu, N. E. Jewell-Larsen, C. Sticht, I. A. Krichtafovitch, and A. V. Mamishev, "Heat transfer enhancement measurement for microfabricated electrostatic fluid accelerators," in *2008 Twenty-fourth Annual IEEE Semiconductor Thermal Measurement and Management Symposium*, pp. 32–37, 2008.

[54] A. Ongkodjojo, R. Roberts, A. Abramson, and N. Tien, "Highly efficient ionic wind-based cooling microfabricated device for microchip cooling applications," *2010 Solid-State, Actuators, and Microsystems Workshop Technical Digest*, 2010.

[55] A. Ongkodjojo, D. Li, R. C. Roberts, Q. Liu, and N. C. Tien, "Modeling and measurement of microfabricated corona discharge structures," in *2008 3rd IEEE International Conference on Nano/Micro Engineered and Molecular Systems*, pp. 932–937, 2008.

[56] A. O. Ong, A. R. Abramson, and N. C. Tien, "Optimized and microfabricated ionic wind pump array as a next generation solution for electronics cooling systems," in *13th*

InterSociety Conference on Thermal and Thermomechanical Phenomena in Electronic Systems, pp. 1306–1311, 2012.

[57] D. Drew, D. S. Contreras, and K. S. J. Pister, "First thrust from a microfabricated atmospheric ion engine," in *2017 IEEE 30th International Conference on Micro Electro Mechanical Systems (MEMS)*, pp. 346–349, 2017.

[58] D. Drew and K. Pister, "Geometric optimization of microfabricated silicon electrodes for corona discharge-based electrohydrodynamic thrusters," *Micromachines*, vol. 8, no. 5, p. 141, 2017.

[59] D. S. Drew and K. S. J. Pister, "First takeoff of a flying microrobot with no moving parts," in *2017 International Conference on Manipulation, Automation and Robotics at Small Scales (MARSS)*, pp. 1–5, 2017.

[60] R. Tirumala, Y. Li, D. Pohlman, and D. Go, "Corona discharges in sub-millimeter electrode gaps," *Journal of Electrostatics*, vol. 69, no. 1, p. 36–42, 2011.

[61] P. Pai and M. Tabib-Azar, "Sub 3-micron gap microplasma fet with 50 v turn-on voltage," *2014 IEEE 27th International Conference on Micro Electro Mechanical Systems (MEMS)*, 2014.

[62] F. W. Peek, *Dielectric phenomena in high voltage engineering.* 1929.

[63] R. Tirumala, *Corona discharges in Asymmetric Electric Fields and its impact on Ionic Wind Generation*. PhD thesis, University of Notre Dame, 2013.

[64] D. S. Drew, *The Ionocraft: Flying Microrobots With No Moving Parts*. PhD thesis, University of California at Berkeley, 2018.

[65] J. S. Townsend, *Electricity in gases*. Oxford University Press, 1915.

[66] D. B. Go and D. A. Pohlman, "A mathematical model of the modified paschen's curve for breakdown in microscale gaps," *Journal of Applied Physics*, vol. 107, no. 10, 2010.

[67] M. Tabib-Azar and P. Pai, "Microplasma field effect transistors," *Micromachines*, vol. 8, no. 4, p. 117, 2017.

[68] N. Jewell-Larsen, E. Tran, I. Krichtafovitch, and A. Mamishev, "Design and optimization of electrostatic fluid accelerators," *IEEE Transactions on Dielectrics and Electrical Insulation*, vol. 13, no. 1, p. 191–203, 2006.

[69] K. N. KIOUSIS, A. X. MORONIS, and E. D. FYLLADITAKIS, "Finite element analysis method for detection of the corona dischargeinception voltage in a wire-cylinder arrangement," in *Recent Advances in Finite Differences and Applied Computational Mathematics*, pp. 188–193.

[70] Z. Chen, "The experimental investigation of corona discharge induced wall jet," Master's thesis, University of Washington, Seattle, WA, 2019.

[71] R. S. Vaddi, Y. Guan, A. Mamishev, and I. Novosselov, "Analytical model for electrohydrodynamic thrust," *Proceedings of the Royal Society A: Mathematical, Physical and Engineering Sciences*, vol. 476, no. 2241, 2020.

[72] C. Xu, H. Zheng, J. Liu, J. Chu, X. Zeng, R. Sun, and S. Liu, "Enhanced cooling of led filament bulbs using an embedded tri-needle/ring ionic wind device," *Energies*, vol. 13, no. 11, p. 3008, 2020.

[73] J. Zhang, L. Kong, J. Qu, S. Wang, and Z. Qu, "Numerical and experimental investigation on configuration optimization of the large-size ionic wind pump," *Energy*, vol. 171, p. 624–630, Jan 2019.

[74] A. Ongkodjojo, A. R. Abramson, and N. C. Tien, "Design, modeling, and optimization for highly efficient ionic wind-based cooling microfabricated devices," *Volume 4: Electronics and Photonics*, 2010.

[75] N. A. Kaptsov, *Elektricheskie Yavleniya v Gazakh i Vakuume*. Moscow: OGIZ, 1947.

[76] A. A. Ramadhan, N. Kapur, J. Summers, and H. Thompson, "Numerical modelling of electrohydrodynamic airflow induced in a wire-to-grid channel," *Journal of Electrostatics*, vol. 87, p. 123–139, Apr 2017.

[77] "Coin specifications." Available at `https://www.usmint.gov/learn/coin-and-medal-programs/coin-specifications`.

[78] "25 cents." Available at `https://www.mint.ca/en/discover/canadian-circulation/25-cents`.

[79] T. Zhang, Y. Zhang, Q. Ji, B. Li, and J. Ouyang, "Characteristics and underlying physics of ionic wind in dc corona discharge under different polarities*," *Chinese Physics B*, vol. 28, no. 7, p. 075202, 2019.

[80] J. Primas, M. Malík, P. Pokorný, J. Novák, P. Parma, F. Sanetrník, and P. Schovanec, "Detailed analysis of airflow generated by high voltage on a point-tube electrode geometry," *Fluids*, vol. 8, no. 4, p. 115, 2023.

[81] I. E. Rebrov and V. Y. Khomich, "Formation of electrohydrodynamic flow in corona discharge of a three-cascade electrode system with serial and alternating connection," *Plasma Physics Reports*, vol. 47, p. 105–109, Feb 2021.

[82] Y. Guan, R. S. Vaddi, A. Aliseda, and I. Novosselov, "Experimental and numerical investigation of electrohydrodynamic flow in a point-to-ring corona discharge," *Physical Review Fluids*, vol. 3, no. 4, 2018.

[83] C. L. Nelson and D. S. Drew, "High aspect ratio multi-stage ducted electroaerodynamic thrusters for micro air vehicle propulsion," Tech. Rep. arXiv:2308.09840v1, ArXiV, 2023.

[84] M. F. Cabanas, F. P. González, A. S. González, M. R. García, and M. G. Melero, "Analysis of the efficiency of the electrohydrodynamic propulsion based on the biefeld-brown effect for manned and unmanned aircrafts," *Applied Sciences*, vol. 12, no. 6, p. 2997, 2022.

[85] C. Kim, D. Park, K. Noh, and J. Hwang, "Velocity and energy conversion efficiency characteristics of ionic wind generator in a multistage configuration," *Journal of Electrostatics*, vol. 68, no. 1, p. 36–41, 2010.

[86] D. S. Drew and S. Follmer, "High force density multi-stage electrohydrodynamic jets using folded laser microfabricated electrodes," in *2021 21st International Conference on Solid-State Sensors, Actuators and Microsystems (Transducers)*, pp. 54–57, 2021.

[87] J. Leng, Z. Liu, X. Zhang, D. Huang, J. Huang, M. Qi, and X. Yan, "Electrohydrodynamic thrust with no combustion emissions and noises in a centimeter-scale point-to-grid configuration," *IOP Conference Series: Earth and Environmental Science*, vol. 675, no. 1, p. 012015, 2021.

[88] C. K. Gilmore and S. R. Barrett, "Electrohydrodynamic thrust density using positive corona-induced ionic winds for in-atmosphere propulsion," *Proceedings of the Royal Society A: Mathematical, Physical and Engineering Sciences*, vol. 471, no. 2175, p. 20140912, 2015.

[89] J.-S. Chang, H. Tsubone, G. D. Harvel, and K. Urashima, "Narrow-flow-channel-driven ehd gas pump for an advanced thermal management of microelectronics," *IEEE Transactions on Industry Applications*, vol. 46, no. 3, pp. 1151–1158, 2010.

[90] H. Tsubone, J. Ueno, B. Komeili, S. Minami, G. Harvel, K. Urashima, C. Ching, and J. Chang, "Flow characteristics of dc wire-non-parallel plate electrohydrodynamic gas pumps," *Journal of Electrostatics*, vol. 66, p. 115–121, Oct 2007.

[91] M. Rickard, D. Dunn-Rankin, F. Weinberg, and F. Carleton, "Characterization of ionic wind velocity," *Journal of Electrostatics*, vol. 63, no. 6–10, p. 711–716, 2005.

[92] W. Qiu, L. Xia, L. Yang, Q. Zhang, L. Xiao, and L. Chen, "Experimental study on the velocity and efficiency characteristics of a serial staged needle array-mesh type ehd gas pump," *Plasma Science and Technology*, vol. 13, no. 6, p. 693–697, 2011.

[93] W. Qiu, L. Xia, X. Tan, and L. Yang, "The velocity characteristics of a serial-staged ehd gas pump in air," *IEEE Transactions on Plasma Science*, vol. 38, no. 10, pp. 2848–2853, 2010.

[94] S. Mukherjee, M. Y. Elsayed, H. H. Tawfik, and M. N. El-Gamal, "A fabrication method for realizing vertically aligned silicon nanowires featuring precise dimension control." Manuscript to be submitted for publication, 2024.

[95] G. Zheng, W. Lu, S. Jin, and C. M. Lieber, "Synthesis and fabrication of high-performance n-type silicon nanowire transistors," *Advanced Materials*, vol. 16, no. 21, p. 1890–1893, 2004.

[96] X. Song, T. Zhang, L. Wu, R. Hu, W. Qian, Z. Liu, J. Wang, Y. Shi, J. Xu, K. Chen, and et al., "Highly stretchable high-performance silicon nanowire field effect transistors integrated on elastomer substrates," *Advanced Science*, vol. 9, no. 9, p. 2105623, 2022.

[97] Y. Cui, Z. Zhong, D. Wang, W. U. Wang, and C. M. Lieber, "High performance silicon nanowire field effect transistors," *Nano Letters*, vol. 3, no. 2, p. 149–152, 2003.

[98] Y. Huang, X. Duan, Y. Cui, L. J. Lauhon, K.-H. Kim, and C. M. Lieber, "Logic gates and computation from assembled nanowire building blocks," *Science*, vol. 294, no. 5545, p. 1313–1317, 2001.

[99] E. Garnett and P. Yang, "Light trapping in silicon nanowire solar cells," *Nano Letters*, vol. 10, no. 3, p. 1082–1087, 2010.

[100] Y. Zhang and H. Liu, "Nanowires for high-efficiency, low-cost solar photovoltaics," *Crystals*, vol. 9, no. 2, p. 87, 2019.

[101] J. Yun, J.-H. Ahn, D.-I. Moon, Y.-K. Choi, and I. Park, "Joule-heated and suspended silicon nanowire based sensor for low-power and stable hydrogen detection," *ACS Applied Materials amp;amp; Interfaces*, vol. 11, no. 45, p. 42349–42357, 2019.

[102] W. Chen, H. Yao, C. H. Tzang, J. Zhu, M. Yang, and S.-T. Lee, "Silicon nanowires for high-sensitivity glucose detection," *Applied Physics Letters*, vol. 88, no. 21, 2006.

[103] N. S. Mohammad, "Understanding quantum confinement in nanowires: Basics, applications and possible laws," *Journal of Physics: Condensed Matter*, vol. 26, no. 42, p. 423202, 2014.

[104] "The all-new amprius 500 wh/kg battery platform is here," 2023. `https://amprius.com/the-all-new-amprius-500-wh-kg-battery-platform-is-here/` [Accessed: (August, 2023)].

[105] S. Chang, G. Lee, and Y. Song, "Recent advances in vertically aligned nanowires for photonics applications," *Micromachines*, vol. 11, no. 8, p. 726, 2020.

[106] R. A. Puglisi, C. Bongiorno, S. Caccamo, E. Fazio, G. Mannino, F. Neri, S. Scalese, D. Spucches, and A. La Magna, "Chemical vapor deposition growth of silicon nanowires with diameter smaller than 5 nm," *ACS Omega*, vol. 4, no. 19, p. 17967–17971, 2019.

[107] S. Acharya and A. Kottantharayil, "Vls growth of silicon nanowires in cold wall cat-cvd chamber," in *2014 IEEE 2nd International Conference on Emerging Electronics (ICEE)*, pp. 1–4, 2014.

[108] K.-Q. Peng, Y.-J. Yan, S.-P. Gao, and J. Zhu, "Synthesis of large-area silicon nanowire arrays via self-assembling nanoelectrochemistry," *Advanced Materials*, vol. 14, no. 16, p. 1164, 2002.

[109] S. Jana, S. Mondal, and S. R. Bhattacharyya, "Wetting and surface energy of vertically aligned silicon nanowires," *Journal of Nanoscience and Nanotechnology*, vol. 13, no. 6, p. 3983–3989, 2013.

[110] F. J. Wendisch, M. Rey, N. Vogel, and G. R. Bourret, "Large-scale synthesis of highly uniform silicon nanowire arrays using metal-assisted chemical etching," *Chemistry of Materials*, vol. 32, no. 21, p. 9425–9434, 2020.

[111] Z. Huang, H. Fang, and J. Zhu, "Fabrication of silicon nanowire arrays with controlled diameter, length, and density," *Advanced Materials*, vol. 19, no. 5, p. 744–748, 2007.

[112] C.-Y. Chen and Y.-R. Liu, "Exploring the kinetics of ordered silicon nanowires with the formation of nanogaps using metal-assisted chemical etching," *Phys. Chem. Chem. Phys.*, vol. 16, p. 26711–26714, Nov 2014.

[113] M. N. Nor, U. Hashim, N. H. Halim, N. H. Hamat, M. Rusop, R. Y. Subban, N. Kamarulzaman, and W. T. Wui, "Top-down approach: Fabrication of silicon nanowires using scanning electron microscope based electron beam lithography method and inductively coupled plasma-reactive ion etching," *AIP Conference Proceedings*, Mar 2010.

[114] M.-C. Sun, G. Kim, J. H. Lee, H. Kim, S. W. Kim, H. W. Kim, J.-H. Lee, H. Shin, and B.-G. Park, "Patterning of si nanowire array with electron beam lithography for sub-22nm si nanoelectronics technology," *Microelectronic Engineering*, vol. 110, p. 141–146, 2013.

[115] M. Ko, S.-H. Baek, B. Song, J.-W. Kang, S.-A. Kim, and C.-H. Cho, "Periodically diameter-modulated semiconductor nanowires for enhanced optical absorption," *Advanced Materials*, vol. 28, no. 13, p. 2504–2510, 2016.

[116] P. Fischer and S. Chou, "Rie of sub-50 nm high aspect-ratio pillars, ridges, and trenches in silicon and silicon-germanium," *Microelectronic Engineering*, vol. 21, no. 1–4, p. 311–314, 1993.

[117] M. Poudineh, Z. Sanaee, A. Gholizadeh, S. Soleimani, and S. Mohajerzadeh, "Formation of highly ordered silicon nanowires by a high-speed deep etching," *IEEE Transactions on Nanotechnology*, vol. 12, no. 5, pp. 712–718, 2013.

[118] C. Pang, Z. Zhao, L. Du, and Z. Fang, "Adhesive bonding with su-8 in a vacuum for capacitive pressure sensors," *Sensors and Actuators A: Physical*, vol. 147, p. 672–676, Jun 2008.

[119] D. Admassu, T. Durowade, W. Gao, S. Velicu, and S. Sivananthan, "Adhesive wafer bonding of micro-actuators with su-8 photoresist," *Microsystem Technologies*, vol. 27, no. 9, p. 3293–3297, 2020.

[120] L. Yu, C. Iliescu, F. Tay, and B. Chen, "SU8 adhesive bonding using contact imprinting," in *2006 International Semiconductor Conference*, vol. 1, pp. 189–192, 2006.

[121] K.-J. Wang, H.-C. Sun, C.-L. Li, G.-D. Wang, and H.-W. Zhu, "Thermal management of the hotspots in 3-D integrated circuits," *Thermal Science*, vol. 22, no. 4, p. 1685–1690, 2018.

[122] K. Salah, "Survey on 3D-ICs thermal modeling, analysis, and management techniques," in *2017 IEEE 19th Electronics Packaging Technology Conference (EPTC)*, pp. 1–4, 2017.

[123] J. H. Lau and T. G. Yue, "Thermal management of 3D IC integration with tsv (through silicon via)," in *2009 59th Electronic Components and Technology Conference*, pp. 635–640, 2009.

[124] W. Brown, A. Malshe, T. Railkar, T. Lenihan, J. Stone, W. Sommers, and L. Schaper, "Thermal management issues and evaluation of a novel, flexible substrate, 3-dimensional (3-D) packaging concept," in *Proceedings. 1998 International Conference on Multichip Modules and High Density Packaging (Cat. No.98EX154)*, pp. 135–140, 1998.

[125] N. Y. Meitei, K. L. Baishnab, and G. Trivedi, "Fast power density aware three-dimensional integrated circuit floorplanning for hard macroblocks using best

operator combination genetic algorithm," *International Journal of Circuit Theory and Applications*, 2023.

[126] D. Drew and K. Pister, "Takeoff of a flying microrobot with cots sensor payload using electrohydrodynamic thrust produced by sub-millimeter corona discharge," *2018 Solid-State, Actuators, and Microsystems Workshop Technical Digest*, 2018.

[127] A. O. Ong, *ELECTROHYDRODYNAMIC MICROFABRICATED IONIC WIND PUMPS FOR ELECTRONICS COOLING APPLICATIONS*. PhD thesis, CASE WESTERN RESERVE UNIVERSITY, 2013.

[128] L. Wu, A. Lin, B. Lu, B. Zheng, M. Guo, and G. Hui, "Experimental study of corona discharge with multi-walled carbon nanotubes electrode," in *2009 IEEE International Conference on Robotics and Biomimetics (ROBIO)*, pp. 2146–2150, 2009.

[129] J. Chen, "Nanoscale corona discharge electrode," March 2009.